


**Higher-order Weyl superconductors with anisotropic Weyl-point connectivity**W. B. Rui,<sup>1,\*</sup> Song-Bo Zhang<sup>1,2,†</sup>, Moritz M. Hirschmann<sup>1,3</sup>, Zhen Zheng,<sup>1</sup> Andreas P. Schnyder,<sup>3</sup> Björn Trauzettel,<sup>2</sup> and Z. D. Wang<sup>1,‡</sup><sup>1</sup>*Department of Physics and HKU-UCAS Joint Institute for Theoretical and Computational Physics at Hong Kong, The University of Hong Kong, Pokfulam Road, Hong Kong, China*<sup>2</sup>*Institute for Theoretical Physics and Astrophysics, University of Würzburg, D-97074 Würzburg, Germany*<sup>3</sup>*Max-Planck-Institute for Solid State Research, Heisenbergstrasse 1, D-70569 Stuttgart, Germany* (Received 21 September 2020; revised 21 February 2021; accepted 19 April 2021; published 19 May 2021)

Weyl superconductors feature Weyl points at zero energy in the three-dimensional Brillouin zone and arc states that connect the projections of these Weyl points on the surface. We report that higher-order Weyl superconductors can be realized in odd-parity topological superconductors with time-reversal symmetry being broken by periodic driving. Different from conventional Weyl points, the higher-order Weyl points in the bulk separate 2D first- and second-order topological phases, while on the surface, their projections are connected not only by conventional surface Majorana arcs but also by hinge Majorana arcs. Strikingly, without the protection by a Chern number, the hinge Majorana arcs are anisotropic with respect to surface orientations, forcing a different connectivity of Weyl points for a rotated surface. We identify such anisotropic Weyl-point connectivity as a characteristic feature of higher-order Weyl materials. Moreover, with time-reversal symmetry being broken, the higher-order hinge Majorana arcs are spin polarized, which offers a promising opportunity to observe the anisotropic Weyl-point connectivity with spin-sensitive probes. Besides condensed-matter systems, we provide a feasible experimental setup for realizing our predictions in cold-atom systems.

DOI: [10.1103/PhysRevB.103.184510](https://doi.org/10.1103/PhysRevB.103.184510)**I. INTRODUCTION**

The particular excitations of topological semimetals and nodal superconductors emerge around gapless degeneracies and constitute one of the main research activities in the field of topological materials [1–7]. Typical examples are Weyl and Dirac semimetals or nodal superconductors whose low-energy physics around the gapless points can be described by Weyl or Dirac Hamiltonians [8–15]. Besides exotic quasiparticles in the bulk, the bulk topology of the systems also gives rise to fascinating topological boundary states. Conventionally, in an  $n$ -dimensional topological phase, the topological boundary states are constrained to  $(n - 1)$  dimensions.

Recently, inspired by higher-order topology featuring  $(n - d)$ -dimensional hinge or corner states with  $d \geq 2$  [16–28], new topological phases, termed higher-order topological gapless phases, have attracted increasing interest [29–36]. As an important member of gapless phases, Weyl superconductors must break time-reversal or inversion symmetry [11,12,37,38]. Time-reversal symmetry breaking is particularly important, as most reported first-order (conventional) Weyl superconductors are realized in this way [39–47]. However, so far, there has been no study on higher-order Weyl superconductors (HOWSCs) with broken time-reversal symmetry. The most prominent feature of Weyl materials is that

the projections of Weyl points on the surface are connected by Fermi (Majorana) arcs. Such Weyl-point connectivity is typically isotropic in conventional Weyl materials, because the Chern number enforces orientation independent Fermi arc surface states. Remarkably, we will reveal that the situation is fundamentally different in higher-order Weyl materials and the Weyl-point connectivity becomes *highly anisotropic*, as shown in Fig. 1.

In this paper, we show that HOWSCs with broken time-reversal symmetry can be realized by periodically driving a two-dimensional (2D) second-order odd-parity topological superconductor. The periodic driving breaks time-reversal symmetry and offers an unprecedented and realistic way to extend the 2D superconductor to a third dimension with periodic boundary conditions. Weyl points can be generated in this dynamic process, which split the system into different regions of first- (FOTP) or second-order topological phases (SOTP), leading to a HOWSC. In sharp contrast to the surface Majorana arcs protected by a Chern number in the FOTP regions, the hinge Majorana arcs in the SOTP regions, which are protected by inversion symmetry, depend strongly on the surface orientation due to the higher-order topology. This results in an intriguing and diverse recombination of surface and hinge Majorana arcs upon orientation change, leading to an anisotropic Weyl-point connectivity. By developing an effective boundary theory capable of describing both surface and hinge Majorana arcs, we thoroughly analyze this intricate Weyl-point connectivity of Majorana arcs in every surface orientation. Furthermore, as an important consequence of breaking time-reversal symmetry, higher-order hinge Majorana arcs

\* wenbin.rui@gmail.com

† songbo.zhang@physik.uni-wuerzburg.de

‡ zwang@hku.hk

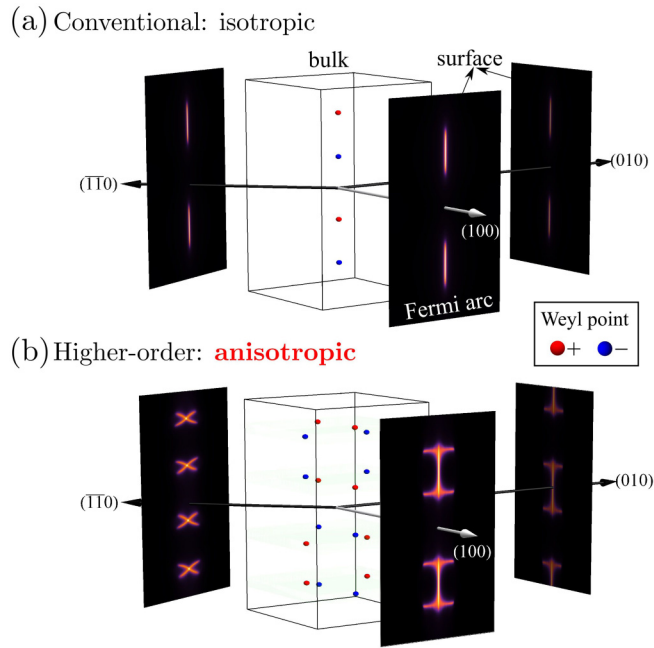


FIG. 1. (a) In conventional Weyl semimetals/superconductors, the Weyl-point connectivity by Fermi arcs is isotropic with respect to surface orientations. (b) In higher-order Weyl semimetals/superconductors, the Weyl-point connectivity is anisotropic due to higher-order topology.

acquire a spin polarization that can be easily manipulated by tuning the phase of the periodic driving. Thus, we suggest detecting the Majorana arcs and the anisotropic Weyl-point connectivity by measuring spin polarization at low energies.

## II. REALIZATION OF HOWSCs

Our starting point is a 2D second-order odd-parity topological superconductor that respects time-reversal symmetry. Different from previous proposals for higher-order topological superconductors [48–71], we consider an interorbital  $s$ -wave pairing potential with a constant magnitude  $\Delta_0$ . The Hamiltonian in momentum space can be written as  $\mathcal{H} = \mathcal{H}_0 + h_\Delta$  with

$$\begin{aligned} \mathcal{H}_0 &= m(\mathbf{k})\tau_z\sigma_z + v \sin k_x s_z \sigma_x + v \sin k_y \tau_z \sigma_y - \mu\tau_z, \\ h_\Delta &= \Delta_0 \tau_y s_y \sigma_x, \end{aligned} \quad (1)$$

where  $m(\mathbf{k}) = M_0 - 2m(\cos k_x + \cos k_y)$  and the Pauli matrices  $\mathbf{s}$ ,  $\boldsymbol{\sigma}$  and  $\boldsymbol{\tau}$  act on spin, orbital, and Nambu spaces, respectively.  $\mu$  is the chemical potential,  $M_0$ , and  $m$  and  $v$  are material dependent parameters. The Hamiltonian is invariant under time-reversal ( $\mathcal{T}$ ) and particle-hole ( $\mathcal{C}$ ) symmetry. The pairing interaction is of odd parity, as indicated by  $\mathcal{P}h_\Delta\mathcal{P}^{-1} = -h_\Delta$  with the inversion operator  $\mathcal{P} = \sigma_z$ . Correspondingly, the BdG Hamiltonian is symmetric under inversion  $\tilde{\mathcal{P}}\mathcal{H}(\mathbf{k})\tilde{\mathcal{P}}^{-1} = \mathcal{H}(-\mathbf{k})$  with  $\tilde{\mathcal{P}} = \tau_z\mathcal{P}$ . Furthermore, spin rotation about the  $z$  axis  $J_z = \tau_z s_z$  is preserved. Due to the second-order topology, our model features two zero-dimensional Majorana Kramers pairs at a disk boundary, which are protected by time-reversal and inversion symmetries.

Next, we show that HOWSCs can be generated on the basis of Eq. (1) through periodic driving. For concreteness, we consider a driving described by a vector potential  $\mathbf{A}(t) = A_0[\cos(\omega t), \sin(\omega t + \phi), 0]$ , where  $\phi$  characterizes the phase shift,  $A_0$  the strength, and  $\omega$  the frequency. It couples to the electrons (holes) via the Peierls substitutions  $\mathbf{k} \rightarrow \mathbf{k} \pm e\mathbf{A}(t)$ . Notably, in condensed-matter systems, the model (1) with the periodic driving  $\mathbf{A}(t)$  can be realized by shedding circularly polarized light (CPL) in  $z$  direction on quantum spin Hall insulators in proximity with odd-parity superconductors. Alternatively, it can be realized in a cold-atom experiment. By using the internal states and layer index to emulate the spins and orbits in cold atoms, respectively, Eq. (1) can be synthesized by the current techniques of laser-assisted tunneling, while  $\mathbf{A}(t)$  can be implemented by artificial non-Abelian gauge fields. We present the details of the realizations in the Appendixes.

To proceed analytically and elucidate our main results, we employ Floquet theory and derive an effective static Hamiltonian, as discussed in the Appendixes. The effective Hamiltonian is obtained on the basis of Eq. (1) and contains a nontrivial correction that preserves spin-rotation symmetry about the  $z$  axis. Explicitly, it reads

$$h(\mathbf{k}) = h_0(\mathbf{k}) + \gamma(\mathbf{k}) \cos \phi, \quad (2)$$

where  $\gamma(\mathbf{k}) = (2m\mathcal{I}/\omega)(v \sin k_x \sigma_x + v \sin k_y \sigma_y - v^2 \sigma_z / 2m)$  and  $h_0(\mathbf{k}) = \tau_z[(m(\mathbf{k}) + m\mathcal{I})\sigma_z + v \sin k_x \sigma_x + v \sin k_y \sigma_y - \mu] - \Delta_0 \tau_x \sigma_x$  with  $\mathcal{I} = e^2 A_0^2$ . The periodic driving breaks time-reversal symmetry. By tuning the phase  $\phi$ , we see that the Majorana zero modes (MZMs) at the disk boundary can jump from the horizontal to vertical positions [insets of Fig. 2(a)].

The model in Eq. (2) is periodic in the parameter  $\phi$ . We may regard it as an extra (third) dimension. Since at each  $\phi$  time-reversal symmetry is broken, the 2D systems for fixed  $\phi$  belong to class A and are characterized by a Chern number [72]. Strikingly, stacking these 2D systems along  $\phi$  direction gives a three-dimensional (3D) Weyl superconductor with 16 Weyl points in the synthetic 3D Brillouin zone, as displayed in Fig. 2(b). These Weyl points can be grouped into four distinct sets.

In Fig. 2(a), we stack the 2D disks with different  $\phi$ , forming a 3D cylinder. The cylinder is finite in  $x$  and  $y$  directions but periodic in  $\phi$  direction. As can be seen by the dimensions of the boundary states, the system splits into two kinds of topological phases: (i) FOTPs within each of the Weyl-point sets, with 2D surface states at the boundary (green belts); (ii) SOTPs between different Weyl-point sets, with one-dimensional (1D) hinge states (red lines). As the Weyl points mediate between the FOTP and SOTPs, we identify the system as an HOWSC.

## III. ANISOTROPIC WEYL-POINT CONNECTIVITY

Figure 3(a) shows the Chern number calculated in  $k_x k_y$  planes for different  $\phi$  in the HOWSC. It takes the nontrivial value of 2 or  $-2$  inside each set of Weyl points (corresponding to the FOTP regions), which leads to conventional surface Majorana arcs. In contrast, it vanishes between neighboring sets (corresponding to the SOTP regions), where hinge Majorana arcs arise [73]. Without the restriction by the Chern number,

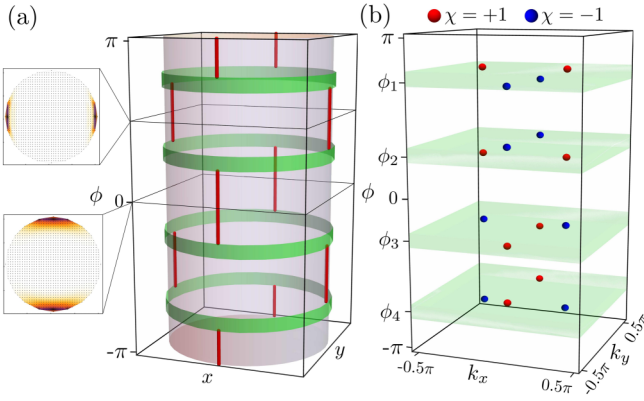


FIG. 2. (a) Schematic of boundary states of HOWSC described by Eq. (2), obtained by stacking the 2D superconductors of Eq. (1) in the third dimension parameterized by  $\phi$  through periodic driving. In the FOTP regions, the boundary states circle around the whole disk boundary (green belts), whereas in the SOTP regions, they form hinge states on 1D lines (red lines). The insets show that by tuning phase  $\phi$  of the vector potential  $\mathbf{A}(t)$ , the position of the Majorana zero modes can be switched. (b) The 16 Weyl points of model (2) in the synthetic 3D Brillouin zone. The red and blue points denote Weyl points with positive and negative chirality  $\chi = \pm 1$ , respectively. The Weyl points are grouped into four sets, denoted by their center positions  $\phi_j$  with  $j \in \{1, 2, 3, 4\}$ . Each set consists of four Weyl points. Their positions divide the Brillouin zone into different topological sectors. We identify FOTPs (green area) within each of the four sets and SOTPs between neighboring sets. The parameters are  $M_0 = 2.20$ ,  $v = 0.74$ ,  $\mu = 0$ ,  $\omega = 1.10$ , and  $\Delta_0 = 0.35$ , in units of  $m$ , with the intensity  $\mathcal{I} = 1.50\omega/(2m)$ . This proposal is realizable in cold-atom experiments (see Appendixes).

hinge Majorana arcs can be anisotropic with respect to surface orientation. In the following, we show that with the hinge Majorana arcs, the Weyl-point connectivity is fundamentally changed and becomes *highly anisotropic* in HOWSCs.

To visualize the Weyl-point connectivity, we calculate the surface density of states for different surface orientations. Remarkably, the form of the Weyl-point connectivity is strongly anisotropic with respect to surface orientation. Three typical cases of (100), (010), and (110) surfaces are displayed in Figs. 3(b)–3(d), respectively. In Fig. 3(b), for the (100) surface, the connectivity exhibits two separated “H” shapes rotated by 90 degrees. In this case, while the surface Majorana arcs form the horizontal bars of the “H” shapes within each Weyl set, the hinge Majorana arcs form the vertical bars and connect the Weyl-point sets  $\phi_1(\phi_3)$  and  $\phi_2(\phi_4)$ . Notably, there are double-hinge Majorana arcs connecting two pairs of Weyl points with opposite chirality. Next, we turn to the (010) surface [Fig. 3(c)]. Although the connectivity still forms two rotated “H” shapes, the vertical bars composed of hinge Majorana arcs now connect different pairs of Weyl-point sets, namely,  $\phi_4(\phi_2)$  and  $\phi_1(\phi_3)$ . Finally, in Fig. 3(d) for the (110) surface, the Weyl points can only be connected by surface Majorana arcs in cross shapes. While surface Majorana arcs can always be observed, the hinge Majorana arcs depend sensitively on surface orientation. Thus, the Weyl-point connectivity is anisotropic.

#### IV. EFFECTIVE BOUNDARY THEORY

For a better understanding of the orientation-dependent connectivity of the Majorana arcs, it is instructive to develop a boundary theory applicable to any surface orientation. To do so, we first derive two boundary states ( $\Psi_{e\uparrow}, \Psi_{h\downarrow}$ ) for each  $\phi$  in the absence of pairing interactions (see Appendixes). Using these boundary states as a basis, the resulting effective boundary Hamiltonian can be obtained as

$$h_{\text{eff}}(\theta) = \begin{pmatrix} |v^+|k_{\parallel} - \mu & \tilde{\Delta}(\theta) \\ \tilde{\Delta}(\theta)^* & -|v^-|k_{\parallel} + \mu \end{pmatrix}, \quad (3)$$

where  $v^{\pm} = v(1 \pm 2m\mathcal{I} \cos \phi/\omega)$ ,  $\theta$  is the angle between the boundary and  $x$  direction, and  $k_{\parallel}$  is the momentum along the boundary (see Fig. 5 in the Appendixes). The projected pairing potential  $\tilde{\Delta}(\theta)$  is obtained as

$$\tilde{\Delta}(\theta) = \frac{i}{2} \mathcal{F} \Delta_0 \text{sgn}(v^-) [\text{sgn}(v^+v^-) e^{i\theta} - e^{-i\theta}], \quad (4)$$

with  $\text{sgn}(\cdot)$  being the sign function. The prefactor  $\mathcal{F}$  stems from the overlap of the boundary state wave functions (see Appendixes). It is unity for  $\cos \phi = 0$  but smaller than 1 in general. The eigenenergies are given by  $E_{\text{eff}} = (|v^+| - |v^-|)k_{\parallel}/2 + \{[(|v^+| + |v^-|)k_{\parallel}/2 - \mu]^2 + |\tilde{\Delta}(\theta)|^2\}^{1/2}$ . The chemical potential  $\mu$  can be absorbed in  $k_{\parallel}$  in the square root, and the band gap is given by  $2|\tilde{\Delta}(\theta)|$ . For simplicity, we set  $\mu$  to zero in the following discussion. Notably, Eq. (3) takes the form of a 1D Dirac Hamiltonian with a Dirac mass  $\tilde{\Delta}(\theta)$ . The mass gaps out the boundary spectrum everywhere, except for isolated values of  $\theta$  where  $\tilde{\Delta}(\theta) = 0$ . This is the reason why the appearance of hinge Majorana arcs depends sensitively on the surface orientation in the SOTPs.

The periodic driving preserves inversion symmetry of the system. Thus Eq. (3) obeys  $\tilde{\mathcal{P}} h_{\text{eff}}(\theta) \tilde{\mathcal{P}}^{-1} = h_{\text{eff}}(\theta + \pi)$ , with  $\tilde{\mathcal{P}} = \sigma_z$  the projected inversion operator, enforcing a constraint on  $\tilde{\Delta}(\theta)$ :  $\tilde{\Delta}(\theta + \pi) = -\tilde{\Delta}(\theta)$ . Obviously,  $\tilde{\Delta}(\theta)$  changes sign when advancing from  $\theta$  to  $\theta + \pi$ , leading to a gapless point along  $\theta$ . The gapless point corresponds to the positions of a hinge Majorana arc. In this regard, the SOTP is protected by inversion symmetry. This result is not restricted to a specific geometry as long as inversion symmetry is preserved. From Eq. (4) we can determine the positions of the gapless points explicitly,

$$\theta = \pi[1 - \text{sgn}(v^+v^-)]/4 + n\pi, \quad n \in \{0, 1\}. \quad (5)$$

When  $2m\mathcal{I}/\omega > 1$ ,  $v^+v^-$  changes sign at  $\phi = \phi_j$  with  $j \in \{1, 2, 3, 4\}$ ,  $\phi_1 = -\phi_4 = \pi - \arccos(\omega/2m\mathcal{I})$  and  $\phi_2 = -\phi_3 = \arccos(\omega/2m\mathcal{I})$ . As a result, the positions in Eq. (5) switch from  $\{0, \pi\}$  to  $\{\pi/2, 3\pi/2\}$ .

Facilitated by the boundary theory, we are now able to explain the anisotropic connectivity of the Majorana arcs obtained numerically in Fig. 3. First, for the (100) surface,  $k_{\parallel} = k_y$  and  $\theta = 0$ . In this case, the vanishing of the mass  $\tilde{\Delta}(\theta)$  in Eq. (4) is determined by  $\text{sgn}(v^+v^-) = +1$ , which gives  $\phi \in (\phi_1, \phi_2] \cup (\phi_3, \phi_4]$ . Thus the hinge Majorana arcs connect the Weyl-point sets  $\phi_1$  with  $\phi_2$  and  $\phi_3$  with  $\phi_4$  at  $k_y = 0$ , as shown by the vertical bars in Fig. 3(b). Second, for the (010) surface with  $k_{\parallel} = k_x$  ( $\theta = \pi/2$ ),  $\tilde{\Delta}(\theta)$  vanishes at  $\text{sgn}(v^+v^-) = -1$ , leading to  $\phi \in (\phi_4, \phi_1] \cup (\phi_2, \phi_3]$ . In this



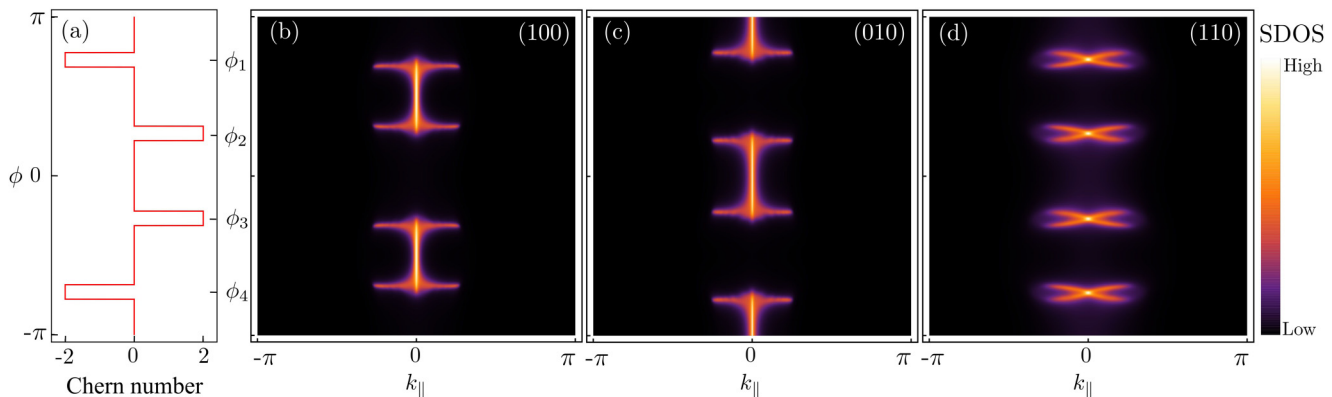


FIG. 3. Anisotropic Weyl-point connectivity due to the higher-order topology. (a) Chern number calculated within the  $k_x k_y$  planes as a function of  $\phi$ . (b)–(d) Surface density of states (SDOS) on the (100), (010), and (110) surfaces, respectively. Surface Majorana arcs connect Weyl points inside each Weyl-point set and form horizontal bars. In contrast, the two hinge Majorana arcs connect Weyl points from two neighboring sets and form vertical bars, which depend strongly on the respective surface orientation. (b) On the (100) surface, the hinge Majorana arcs (vertical bars) connect the Weyl points between  $\phi_1$  ( $\phi_3$ ) and  $\phi_2$  ( $\phi_4$ ), and form two rotated “H” shapes. (c) On the (010) surface, the hinge Majorana arcs connect the Weyl points between  $\phi_4$  ( $\phi_2$ ) and  $\phi_1$  ( $\phi_3$ ). (d) On the (110) surface, the Weyl points are only connected by surface Majorana arcs in cross shapes.

orientation, the hinge Majorana arcs instead connect  $\phi_4$  with  $\phi_1$  and  $\phi_2$  with  $\phi_3$  at  $k_x = 0$ , as shown by the vertical bars in Fig. 3(c). In contrast, for the (110) surface associated with  $\theta = \pi/4$ ,  $\tilde{\Delta}(\theta)$  is always nonzero for all  $\phi$  [Fig. 3(d)]. As a result, there are no hinge arcs connecting the Weyl points.

### V. SPIN-POLARIZED HINGE MAJORANA ARCS

As the periodic driving breaks time-reversal symmetry, we find that by varying  $\phi$ , not only the positions of the MZMs at the boundary of the 2D disk [Fig. 2(a)] can be switched, but also their spin polarizations [74]. Thus the higher-order hinge Majorana arcs, constituted of MZMs, are also spin-polarized, as shown in Figs. 4(b)–4(d).

To elucidate this point, we calculate the spin polarizations of the MZMs on the arcs. Starting with the boundary Hamiltonian Eq. (3), we first obtain the wave functions of the zero-energy modes. From these zero-energy modes, two MZMs can then be derived. Their wave functions in the Nambu and spin basis ( $\Psi_{e\uparrow}, \Psi_{e\downarrow}, \Psi_{h\uparrow}, \Psi_{h\downarrow}$ ) can be written as  $\Psi_1 \propto [e^{i\theta} \text{sgn}(v^+) \sqrt{|v^-|}, i \sqrt{|v^+|}, e^{-i\theta} \text{sgn}(v^-) \sqrt{|v^-|}, -i \sqrt{|v^+|}]^T$  and  $\Psi_2 \propto [ie^{i\theta} \text{sgn}(v^+) \sqrt{|v^-|}, \sqrt{|v^+|}, -ie^{-i\theta} \text{sgn}(v^-) \sqrt{|v^-|}, \sqrt{|v^+|}]^T$  (see Appendixes). The angular positions  $\theta$  are either  $\{0, \pi\}$  or  $\{\pi/2, 3\pi/2\}$ , depending on  $\phi$ , as we have shown before. The spin polarization of the Majorana zero modes can be calculated as  $\langle \hat{S}_j \rangle = \langle \Psi_j | \hat{s} | \Psi_j \rangle$ , where  $j \in \{1, 2\}$  and  $\hat{s} = \hbar(\tau_0 + \tau_z) \mathbf{s} / 2$ . We find that the two MZMs have always opposite spins in  $x$  and  $y$  directions. Thus together they yield vanishing  $\langle \hat{S}_x \rangle = \langle \hat{S}_y \rangle = 0$  at the boundary. In contrast, for the  $z$  component, we find the spin polarization for the MZMs,

$$\langle \hat{S}_z \rangle = \frac{\hbar}{2} \frac{|v^-| - |v^+|}{|v^-| + |v^+|}, \quad (6)$$

which is independent of  $\theta$ . As  $v^{\pm}$  depends on  $\phi$ , the spin polarization changes along the hinge Majorana arcs.

Next we explain the spin polarization of Majorana arcs, with the aid of the phase diagram of the MZMs shown in

Fig. 4(a). As indicated by dashed lines, the spin polarization  $\langle \hat{S}_z \rangle$  splits into spin-up and spin-down regions with the border at  $\phi = \pm\pi/2$  where the correction  $\gamma(\mathbf{k}) \cos \phi$  in Eq. (2), induced by the periodic driving, vanishes and time-reversal symmetry is restored.  $\langle \hat{S}_z \rangle$  is an even function of  $\phi$  while it is an odd function of  $\phi - \pi/2$ . In the vicinity of  $\phi = \pi/2$ , it grows linearly with increasing  $\phi$ ,  $\langle \hat{S}_z \rangle \approx (2\hbar m \mathcal{I} / \omega)(\phi - \pi/2)$ . The spin polarization approaches its maximal value in regions where  $v^+$  or  $v^-$  become zero, which is in the

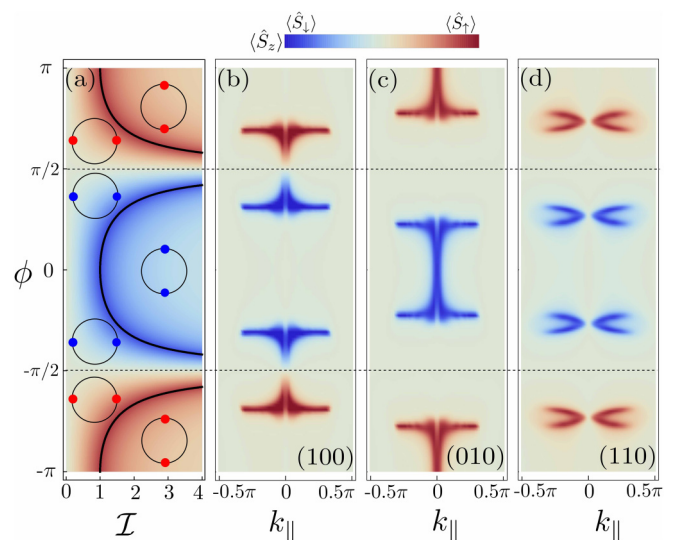


FIG. 4. Spin polarization of Majorana arcs. (a) The phase diagram of MZMs, colored by their spin polarization calculated with Eq. (6). The thick solid lines separate different SOTPs. The locations and polarizations of the MZMs on a 2D disk are sketched by the insets. (b), (c), and (d) display the spin polarization of Majorana arcs in three representative surface orientations corresponding to Figs. 3(b), 3(c), and 3(d), respectively. The spin polarization splits into spin-up and spin-down regions with the border at  $\phi = \pm\pi/2$ . Here  $\mathcal{I}$  is given in units of  $\omega/(2m)$ .

vicinity of Weyl points as indicated by the thick solid lines in Fig. 4(a). These features are generic and apply independent of the surface in any surface orientation. We emphasize that while the MZMs are charge neutral, their spin polarization is measurable by spin-polarized scanning tunneling spectroscopy [75,76], which allows us to detect the Majorana arcs and the anisotropic Weyl-point connectivity.

## VI. CONCLUSIONS

We have proposed to realize time-reversal symmetry broken HOWSCs in second-order topological superconductors with odd-parity pairing potential by periodic driving in condensed-matter and cold-atom experiments. We have revealed an important characteristic feature of higher-order Weyl materials, namely, the anisotropic Weyl-point connectivity of the surface and hinge Majorana arcs. The anisotropic Weyl-point connectivity can be measured by spin-polarized scanning tunneling spectroscopy, as the higher-order hinge Majorana arcs possess finite spin polarization induced by periodic driving.

## ACKNOWLEDGMENTS

This work was supported by the Key-Area Research and Development Program of Guangdong Province (Grant No. 2019B030330001), the CRF (No. C6005-17G) of Hong Kong, the DFG (SPP1666 and SFB1170 “ToCoTronics”), the Würzburg-Dresden Cluster of Excellence ct.qmat (EXC2147, Project ID 390858490), and the Elitenetzwerk Bayern Graduate School on “Topological Insulators”. Z.D.W. also thanks support from Guangdong-Hong Kong Joint Laboratory of Quantum Matter.

## APPENDICES

Here we discuss the symmetries of the 2D second-order odd-parity topological superconductors (Appendix A), present the derivation of the static effective Hamiltonian for higher-order Weyl superconductors by applying Floquet theory (Appendix B), give the details of the effective boundary theory (Appendix C), and compute the wave functions and spin polarizations of Majorana zero modes (Appendix D). We discuss the candidate materials for condensed-matter realizations (Appendix E). We show in detail the experimental setup for realizing our theory in cold-atom systems (Appendix F). Finally, we give detailed suggestions for cold-atom systems which can be readily carried out experimentally (Appendix G).

### APPENDIX A: ODD-PARITY SECOND-ORDER TOPOLOGICAL SUPERCONDUCTORS AND THEIR SYMMETRIES

The BdG Hamiltonian of second-order topological superconductors with an odd-parity pairing potential is given by  $H = \sum_{\mathbf{k}} \Phi_{\mathbf{k}}^{\dagger} \mathcal{H}(\mathbf{k}) \Phi_{\mathbf{k}}$ , where the spinor is  $\Phi_{\mathbf{k}}^{\dagger} = (c_{a,\mathbf{k}\uparrow}^{\dagger}, c_{b,\mathbf{k}\uparrow}^{\dagger}, c_{a,\mathbf{k}\downarrow}^{\dagger}, c_{b,\mathbf{k}\downarrow}^{\dagger}, c_{a,-\mathbf{k}\uparrow}, c_{b,-\mathbf{k}\uparrow}, c_{a,-\mathbf{k}\downarrow}, c_{b,-\mathbf{k}\downarrow})$ , with the subscripts  $\{a, b\}$  denoting two different orbitals, and

$$\mathcal{H}(\mathbf{k}) = \begin{pmatrix} \Xi_0(\mathbf{k}) & \Delta \\ \Delta^{\dagger} & -\Xi_0^*(-\mathbf{k}) \end{pmatrix}. \quad (\text{A1})$$

$\Xi_0(\mathbf{k})$  is the Hamiltonian describing a noninteracting quantum spin Hall (QSH) insulator and  $\Delta(\mathbf{k})$  is the pairing potential. They can be written explicitly as

$$\Xi_0(\mathbf{k}) = \begin{pmatrix} m(\mathbf{k}) & K_-(\mathbf{k}) & 0 & 0 \\ K_+(\mathbf{k}) & -m(\mathbf{k}) & 0 & 0 \\ 0 & 0 & m(\mathbf{k}) & -K_+(\mathbf{k}) \\ 0 & 0 & -K_-(\mathbf{k}) & -m(\mathbf{k}) \end{pmatrix} - \mu \hat{\Gamma},$$

$$\Delta = \begin{pmatrix} 0 & 0 & 0 & -\Delta_0 \\ 0 & 0 & -\Delta_0 & 0 \\ 0 & \Delta_0 & 0 & 0 \\ \Delta_0 & 0 & 0 & 0 \end{pmatrix}, \quad (\text{A2})$$

where  $K_{\pm}(\mathbf{k}) = v(\sin k_x \pm i \sin k_y)$  and  $m(\mathbf{k}) = M_0 - 2m(\cos k_x + \cos k_y)$ . As shown by Eq. (1) in the main text, the Hamiltonian can also be written in terms of Pauli matrices  $\mathcal{H}(\mathbf{k}) = \mathcal{H}_0(\mathbf{k}) + h_{\Delta}$ , where  $\mathcal{H}_0(\mathbf{k}) = m(\mathbf{k})\tau_z\sigma_z + v \sin k_x s_z \sigma_x + v \sin k_y \tau_z \sigma_y - \mu \tau_z$  and  $h_{\Delta} = \Delta_0 \tau_y s_y \sigma_x$ . The Pauli matrices  $\mathbf{s}$ ,  $\boldsymbol{\sigma}$ , and  $\boldsymbol{\tau}$  act on spin, orbital, and Nambu spaces, respectively. Note that the pairing potential is of odd parity and satisfies  $\mathcal{P}h_{\Delta}\mathcal{P}^{-1} = -h_{\Delta}$ , with  $\mathcal{P} = \sigma_z$  the conventional inversion operator. The BdG Hamiltonian satisfies  $\tilde{\mathcal{P}}\mathcal{H}(\mathbf{k})\tilde{\mathcal{P}}^{-1} = \mathcal{H}(-\mathbf{k})$  but  $\mathcal{P}\mathcal{H}(\mathbf{k})\mathcal{P}^{-1} \neq \mathcal{H}(-\mathbf{k})$ , where  $\tilde{\mathcal{P}} = \tau_z \mathcal{P}$ . Thus the combined symmetry  $\tilde{\mathcal{P}}$  can be regarded as an effective inversion for odd-parity superconductors [77].

The BdG Hamiltonian is also invariant under time-reversal and particle-hole transformation, as verified by the following relations:

$$\mathcal{T}\mathcal{H}(\mathbf{k})\mathcal{T}^{-1} = \mathcal{H}(-\mathbf{k}), \quad \mathcal{T} = i s_y \mathcal{K},$$

$$\mathcal{C}\mathcal{H}(\mathbf{k})\mathcal{C}^{-1} = -\mathcal{H}(-\mathbf{k}), \quad \mathcal{C} = \tau_x \mathcal{K}, \quad (\text{A3})$$

where  $\mathcal{K}$  is the complex conjugate operator. In addition, the pairing potential does not break the SU(2) spin rotation symmetry in  $z$  direction. Thus the BdG Hamiltonian respects spin rotation symmetry, i.e.,

$$[J_z, \mathcal{H}(\mathbf{k})] = 0, \quad \text{and} \quad J_z = \begin{pmatrix} s_z & \\ & -s_z^* \end{pmatrix} = \tau_z s_z. \quad (\text{A4})$$

### APPENDIX B: FLOQUET THEORY

We consider periodic driving by circularly polarized light (CPL) which is shed to the sample in  $z$  direction and described by the periodic vector potential  $\mathbf{A}(t) = A_0[\cos(\omega t), \sin(\omega t + \phi), 0]$ . Hence the choices of phase shift of light  $\phi = 0$  and  $\phi = \pi$  correspond to right-handed and left-handed CPL, respectively. The vector potential enters into the BdG Hamiltonian in Eq. (A1) as

$$\mathcal{H}(\mathbf{k}) = \begin{pmatrix} \Xi_0(\mathbf{k} + e\mathbf{A}) & \Delta \\ \Delta^{\dagger} & -\Xi_0^*(-\mathbf{k} + e\mathbf{A}) \end{pmatrix}. \quad (\text{B1})$$

The vector potential  $\mathbf{A}(t)$  turns the Hamiltonian periodic in time,  $\mathcal{H}(\mathbf{k}, t) = \mathcal{H}(\mathbf{k}, t + T)$ , with the periodicity  $T = 2\pi/\omega$ . The periodic Hamiltonian can be expanded as  $\mathcal{H}(\mathbf{k}, t) = \mathcal{H}_0(\mathbf{k}) + \sum_{n \geq 1} \mathcal{H}_n(\mathbf{k}) e^{in\omega t} + \mathcal{H}_{-n}(\mathbf{k}) e^{-in\omega t}$ . To proceed analytically, we use the Hamiltonian in the continuum limit  $\mathcal{H}(\mathbf{k}) = m(\mathbf{k})\tau_z\sigma_z + v k_x s_z \sigma_x + v k_y \tau_z \sigma_y - \mu \tau_z + \Delta_0 \tau_y s_y \sigma_x$  with  $m(\mathbf{k}) = m_0 + m k_x^2 + m k_y^2$  and  $m_0 = M_0 - 4m$ .

After the inclusion of the vector potential, we obtain

$$\begin{aligned}\mathcal{H}_0(\mathbf{k}) &= \tilde{m}(\mathbf{k})\tau_z\sigma_z + vk_x s_z \sigma_x + vk_y \tau_z \sigma_y - \mu\tau_z + \Delta_0 \tau_y s_y \sigma_x, \\ \mathcal{H}_{\pm 1}(\mathbf{k}) &= eA_0 m(k_x \mp ie^{\pm i\phi} k_y)\tau_z\sigma_z + \frac{1}{2}eA_0 v s_z \sigma_x \\ &\quad \mp \frac{i}{2}eA_0 v e^{\pm i\phi} \tau_z \sigma_y, \\ \mathcal{H}_{\pm 2}(\mathbf{k}) &= \frac{1}{4}e^2 A_0^2 m(1 - 2e^{\pm 2i\phi})\tau_z\sigma_z,\end{aligned}\quad (\text{B2})$$

with  $\tilde{m}(\mathbf{k}) = m(\mathbf{k}) + e^2 A_0^2 m$ . Using Floquet theory, an effective static Hamiltonian can be obtained as [78,79]

$$\mathcal{H}_{\text{eff}} = \mathcal{H}_0(\mathbf{k}) + \sum_{n \geq 1} \frac{[\mathcal{H}_{+n}(\mathbf{k}), \mathcal{H}_{-n}(\mathbf{k})]}{n\omega} + \mathcal{O}\left(\frac{1}{\omega^2}\right). \quad (\text{B3})$$

We find that the nontrivial correction term is given by

$$\begin{aligned}\frac{1}{\omega}[\mathcal{H}_{+1}(\mathbf{k}), \mathcal{H}_{-1}(\mathbf{k})] \\ = \cos\phi \frac{2m\mathcal{I}}{\omega} \left[ vk_y \tau_z s_z \sigma_y + vk_x \tau_0 s_0 \sigma_x - \frac{v^2}{2m} \tau_z s_z \sigma_z \right] \\ = \Delta\mathcal{H}(\mathbf{k}) \cos\phi,\end{aligned}\quad (\text{B4})$$

with  $\mathcal{I} = e^2 A_0^2$  being the intensity of light. We restore to the lattice system in the following.

We now focus on the effect from the correction  $\Delta\mathcal{H}(\mathbf{k}) \cos\phi$  induced by CPL in Eq. (B4). Apparently, it is particle-hole symmetric. It also preserves inversion symmetry  $\tilde{\mathcal{P}} = \tau_z \sigma_z$  and  $z$ -directional spin-rotation symmetry  $J_z = \tau_z s_z$ , as shown by

$$\tilde{\mathcal{P}}\Delta\mathcal{H}(\mathbf{k})\tilde{\mathcal{P}}^{-1} = \Delta\mathcal{H}(-\mathbf{k}), \quad (\text{B5})$$

$$[J_z, \Delta\mathcal{H}(\mathbf{k})] = 0. \quad (\text{B6})$$

However, it breaks time-reversal symmetry  $\mathcal{T} = is_y \mathcal{K}$ ,

$$\mathcal{T}\Delta\mathcal{H}(\mathbf{k})\mathcal{T}^{-1} \neq \Delta\mathcal{H}(-\mathbf{k}), \quad (\text{B7})$$

when  $\phi \neq \pi/2, 3\pi/2$ . Therefore the BdG Hamiltonian under the influence of CPL,

$$\tilde{\mathcal{H}}(\mathbf{k}) = \mathcal{H}_0(\mathbf{k}) + \cos\phi \Delta\mathcal{H}(\mathbf{k}), \quad (\text{B8})$$

is invariant under particle-hole transformation, spin-rotation and inversion, but breaks time-reversal symmetry.

Because particle-hole and spin-rotation symmetry are still preserved, the system is protected by their combination of

$$J_z \mathcal{C} = i\tau_y s_z \mathcal{K}, \quad \text{with } (J_z \mathcal{C})^2 = -1. \quad (\text{B9})$$

Similar to time-reversal symmetry, this antiunitary symmetry operator leads to the double degeneracy of Majorana zero modes at the boundary. To see this, we consider the symmetry relation in real space as

$$(J_z \mathcal{C})\tilde{\mathcal{H}}(\mathbf{x})(J_z \mathcal{C})^{-1} = -\tilde{\mathcal{H}}(\mathbf{x}). \quad (\text{B10})$$

Suppose that  $|\psi(\mathbf{x})\rangle$  is the eigenstate of the Hamiltonian with  $\tilde{\mathcal{H}}(\mathbf{x})|\psi(\mathbf{x})\rangle = E(\mathbf{x})|\psi(\mathbf{x})\rangle$ . Due to the above symmetry, we also have  $\tilde{\mathcal{H}}(\mathbf{x})(J_z \mathcal{C})|\psi(\mathbf{x})\rangle = -E(\mathbf{x})(J_z \mathcal{C})|\psi(\mathbf{x})\rangle$ , which means  $(J_z \mathcal{C})|\psi(\mathbf{x})\rangle$  is another eigenstate with energy  $-E(\mathbf{x})$ .  $|\psi(\mathbf{x})\rangle$  and  $(J_z \mathcal{C})|\psi(\mathbf{x})\rangle$  are not the same because if so, we would get a contradiction by applying  $(J_z \mathcal{C})$  twice:  $|\psi(\mathbf{x})\rangle = (J_z \mathcal{C})|\psi(\mathbf{x})\rangle = (J_z \mathcal{C})^2|\psi(\mathbf{x})\rangle = -|\psi(\mathbf{x})\rangle$ . For the Majorana zero modes, they are doubly degenerate, because  $E(\mathbf{x}) = -E(\mathbf{x}) = 0$  results in two independent eigenstates of  $|\psi(\mathbf{x})\rangle$  and  $(J_z \mathcal{C})|\psi(\mathbf{x})\rangle$ .

According to the topological classification described in Ref. [72], the BdG Hamiltonian that preserves  $z$ -directional spin-rotation symmetry but breaks time-reversal symmetry belongs to class A. Due to spin rotation symmetry, the BdG Hamiltonian in Eq. (B8) has a sparse structure with [72,80]

$$\begin{aligned}\mathcal{H}_0(\mathbf{k}) &= \begin{pmatrix} \mathcal{K}_+(\mathbf{k}) + \tilde{m}(\mathbf{k})\sigma_z - \mu\sigma_0 & 0 & 0 & -\Delta_0\sigma_x \\ 0 & -\mathcal{K}_-(\mathbf{k}) + \tilde{m}(\mathbf{k})\sigma_z - \mu\sigma_0 & \Delta_0\sigma_x & 0 \\ 0 & \Delta_0\sigma_x & \mathcal{K}_-(\mathbf{k}) - \tilde{m}(\mathbf{k})\sigma_z + \mu\sigma_0 & 0 \\ -\Delta_0\sigma_x & 0 & 0 & -\mathcal{K}_+(\mathbf{k}) - \tilde{m}(\mathbf{k})\sigma_z + \mu\sigma_0 \end{pmatrix}, \\ \Delta\mathcal{H}(\mathbf{k}) &= \frac{2m\mathcal{I}}{\omega} \begin{pmatrix} \mathcal{K}_+(\mathbf{k}) - \frac{v^2}{2m}\sigma_z & 0 & 0 & 0 \\ 0 & \mathcal{K}_-(\mathbf{k}) + \frac{v^2}{2m}\sigma_z & 0 & 0 \\ 0 & 0 & \mathcal{K}_-(\mathbf{k}) + \frac{v^2}{2m}\sigma_z & 0 \\ 0 & 0 & 0 & \mathcal{K}_+(\mathbf{k}) - \frac{v^2}{2m}\sigma_z \end{pmatrix},\end{aligned}\quad (\text{B11})$$

where  $\mathcal{K}_{\pm}(\mathbf{k}) = v \sin k_x \sigma_x \pm v \sin k_y \sigma_y$ , and  $\tilde{m}(\mathbf{k}) = M_0 - 2m(\cos k_x + \cos k_y) + m\mathcal{I}$ .

Recall that the basis in the second quantized Hamiltonian  $\tilde{H} = \sum_{\mathbf{k}} \Phi_{\mathbf{k}}^{\dagger} \tilde{\mathcal{H}}(\mathbf{k}) \Phi_{\mathbf{k}}$  is  $\Phi_{\mathbf{k}}^{\dagger} = (c_{a,\mathbf{k}\uparrow}^{\dagger}, c_{b,\mathbf{k}\uparrow}^{\dagger}, c_{a,\mathbf{k}\downarrow}^{\dagger}, c_{b,\mathbf{k}\downarrow}^{\dagger}, c_{a,-\mathbf{k}\uparrow}, c_{b,-\mathbf{k}\uparrow}, c_{a,-\mathbf{k}\downarrow}, c_{b,-\mathbf{k}\downarrow})$ . We can rearrange the elements of the  $8 \times 8$  matrix with sparse structure into a  $4 \times 4$  matrix form:  $\tilde{H} = \sum_{\mathbf{k}} \Phi_{\mathbf{k}}^{\dagger} \tilde{\mathcal{H}}(\mathbf{k}) \Phi_{\mathbf{k}} \rightarrow h = \sum_{\mathbf{k}} \tilde{\Phi}_{\mathbf{k}}^{\dagger} h(\mathbf{k}) \tilde{\Phi}_{\mathbf{k}}$  [72,80], where the basis becomes  $\tilde{\Phi}_{\mathbf{k}}^{\dagger} = (c_{a,\mathbf{k}\uparrow}^{\dagger}, c_{b,\mathbf{k}\uparrow}^{\dagger}, c_{a,-\mathbf{k}\downarrow}, c_{b,-\mathbf{k}\downarrow})$ . In this rearrangement,  $\mathcal{H}_0(\mathbf{k}) \rightarrow h_0(\mathbf{k})$  and  $\Delta\mathcal{H}(\mathbf{k}) \rightarrow \gamma(\mathbf{k})$  with  $h_0(\mathbf{k})$  and  $\gamma(\mathbf{k})$ :

$$\begin{aligned}h_0(\mathbf{k}) &= \begin{pmatrix} \mathcal{K}_+(\mathbf{k}) + \tilde{m}(\mathbf{k})\sigma_z - \mu\sigma_0 & -\Delta_0\sigma_x \\ -\Delta_0\sigma_x & -\mathcal{K}_+(\mathbf{k}) - \tilde{m}(\mathbf{k})\sigma_z + \mu\sigma_0 \end{pmatrix} \\ &= \tilde{m}(\mathbf{k})\tau_z\sigma_z + v \sin k_x \tau_z \sigma_x + v \sin k_y \tau_z \sigma_y - \mu\tau_z \sigma_0 - \Delta_0 \tau_x \sigma_x, \\ \gamma(\mathbf{k}) &= \frac{2m\mathcal{I}}{\omega} \begin{pmatrix} \mathcal{K}_+(\mathbf{k}) - \frac{v^2}{2m}\sigma_z & 0 \\ 0 & \mathcal{K}_+(\mathbf{k}) - \frac{v^2}{2m}\sigma_z \end{pmatrix} \\ &= \frac{2m\mathcal{I}}{\omega} \left( v \sin k_x \sigma_x + v \sin k_y \sigma_y - \frac{v^2}{2m} \sigma_z \right),\end{aligned}\quad (\text{B12})$$

where  $\tilde{m}(\mathbf{k}) = m(\mathbf{k}) + m\mathcal{I}$ . Therefore the BdG Hamiltonian can be expressed in the compact form as

$$h(\mathbf{k}) = h_0(\mathbf{k}) + \gamma(\mathbf{k}) \cos \phi \quad (\text{B13})$$

in the basis  $\tilde{\Phi}_{\mathbf{k}}^\dagger$ . Thus we arrive at the effective Hamiltonian stated in Eq. (2) in the main text. Note that under such rearrangement, the inversion symmetry operator becomes  $\mathcal{P}_{\text{eff}} = \tau_z \sigma_z$ . The system is invariant under inversion as

$$\mathcal{P}_{\text{eff}} h(\mathbf{k}) \mathcal{P}_{\text{eff}}^{-1} = h(-\mathbf{k}). \quad (\text{B14})$$

The validity of the rearrangement of the sparse BdG Hamiltonian to the compact form of Eq. (B13) can be seen by block diagonalizing the full Hamiltonian of Eq. (B11) into two blocks with the basis of  $\tilde{\Phi}_{\mathbf{k}}^\dagger = (c_{a,\mathbf{k}\uparrow}^\dagger, c_{b,\mathbf{k}\uparrow}^\dagger, c_{a,-\mathbf{k}\downarrow}, c_{b,-\mathbf{k}\downarrow})$  and  $\tilde{\Phi}'_{\mathbf{k}}^\dagger = (c_{a,\mathbf{k}\downarrow}^\dagger, c_{b,\mathbf{k}\downarrow}^\dagger, c_{a,-\mathbf{k}\uparrow}, c_{b,-\mathbf{k}\uparrow})$ , respectively. The block with the basis  $\tilde{\Phi}_{\mathbf{k}}^\dagger$  is  $h = \sum_{\mathbf{k}} \tilde{\Phi}_{\mathbf{k}}^\dagger h(\mathbf{k}) \tilde{\Phi}_{\mathbf{k}}$  described in Eq. (B13). It is equivalent to the other block  $h' = \sum_{\mathbf{k}} \tilde{\Phi}'_{\mathbf{k}}^\dagger h'(\mathbf{k}) \tilde{\Phi}'_{\mathbf{k}}$  with the basis of  $\tilde{\Phi}'_{\mathbf{k}}^\dagger$ , because the two bases of  $\tilde{\Phi}_{\mathbf{k}}^\dagger$  and  $\tilde{\Phi}'_{\mathbf{k}}^\dagger$  are equivalent to each other with the relation  $\tilde{\Phi}'_{\mathbf{k}}^\dagger = (\tau_x \tilde{\Phi}_{-\mathbf{k}})^\dagger$ . Explicitly, the block of  $h'(\mathbf{k})$  reads

$$h'(\mathbf{k}) = h'_0(\mathbf{k}) + \gamma'(\mathbf{k}) \cos \phi \quad (\text{B15})$$

in the basis of  $\tilde{\Phi}'_{\mathbf{k}}^\dagger$ , where

$$\begin{aligned} h'_0(\mathbf{k}) &= \tilde{m}(\mathbf{k}) \tau_z \sigma_z - v \sin k_x \tau_z \sigma_x + v \sin k_y \tau_z \sigma_y - \mu \tau_z + \Delta_0 \tau_x \sigma_x, \\ \gamma'(\mathbf{k}) &= \frac{2m\mathcal{I}}{\omega} \left( v \sin k_x \sigma_x - v \sin k_y \sigma_y + \frac{v^2}{2m} \sigma_z \right). \end{aligned} \quad (\text{B16})$$

$h'(\mathbf{k})$  in Eq. (B15) and  $h(\mathbf{k})$  in Eq. (B13) are equivalent, as indicated by  $h'(\mathbf{k}) = -\tau_x h^*(-\mathbf{k}) \tau_x^{-1}$ . Therefore we focus on the Hamiltonian in Eq. (B13) in the main text.

### APPENDIX C: EFFECTIVE BOUNDARY HAMILTONIAN

In this section, we derive the effective boundary Hamiltonian in the direction defined by  $\theta = \arctan(k_y/k_x)$  with the center at the origin in the  $k_x k_y$  plane defined by  $\phi$ . To calculate the boundary states along any direction, as shown in Fig. 5, we first transform the coordinates from  $(k_x, k_y)$  to  $(k_{\parallel}, k_{\perp})$ . The relation between  $(k_{\parallel}, k_{\perp})$  and  $(k_x, k_y)$  is given by

$$\begin{pmatrix} k_x \\ k_y \end{pmatrix} = \begin{pmatrix} \sin \theta & \cos \theta \\ -\cos \theta & \sin \theta \end{pmatrix} \begin{pmatrix} k_{\parallel} \\ k_{\perp} \end{pmatrix}. \quad (\text{C1})$$

The boundary states at  $\theta$  can be obtained by taking periodic boundary conditions in  $k_{\parallel}$  direction and open boundary conditions in  $k_{\perp}$  direction.

After the coordinate transformation, the resulting bare Hamiltonian (without pairing potential) from Eq. (B13) in the continuum limit reads

$$h_{\text{bare}}(\mathbf{k}) = \begin{pmatrix} \tilde{m}^-(\mathbf{k}) - \mu & v^+ k_+ e^{-i\theta} & 0 & 0 \\ v^+ k_- e^{i\theta} & -\tilde{m}^-(\mathbf{k}) - \mu & 0 & 0 \\ 0 & 0 & -\tilde{m}^+(\mathbf{k}) + \mu & -v^- k_+ e^{-i\theta} \\ 0 & 0 & -v^- k_- e^{i\theta} & \tilde{m}^+(\mathbf{k}) + \mu \end{pmatrix}, \quad (\text{C2})$$

where  $\mathbf{k} = (k_{\perp}, k_{\parallel})$ ,  $k_{\pm} = k_{\perp} \pm i k_{\parallel}$ ,  $v^{\pm} = v(1 \pm 2m\mathcal{I} \cos \phi / \omega)$ ,  $\tilde{m}^{\pm}(\mathbf{k}) = m_0 + m|\mathbf{k}|^2 + m\mathcal{I} \pm v^2 \mathcal{I} \cos \phi / \omega$ . The basis is  $\tilde{\Phi}_{\mathbf{k}}^\dagger = (c_{a,\mathbf{k}\uparrow}^\dagger, c_{b,\mathbf{k}\uparrow}^\dagger, c_{a,-\mathbf{k}\downarrow}, c_{b,-\mathbf{k}\downarrow})$ . The bare Hamiltonian is in a block-diagonal form, which enables us to investigate each block separately.

First we focus on the upper block in Eq. (C2), which reads

$$h_{\text{upper}}(\mathbf{k}) = \begin{pmatrix} \tilde{m}^-(\mathbf{k}) - \mu & v^+ k_+ e^{-i\theta} \\ v^+ k_- e^{i\theta} & -\tilde{m}^-(\mathbf{k}) - \mu \end{pmatrix}, \quad (\text{C3})$$

and derive the boundary states along the  $x_{\parallel}$  boundary at angle  $\theta$ . Translational symmetry is preserved along this direction. As the wave function of a boundary state decays exponentially away from the boundary ( $k_{\perp}$  direction), the following ansatz

can be adopted:

$$\psi(\mathbf{r}) = e^{ik_{\parallel} x_{\parallel}} e^{\zeta x_{\perp}} \begin{pmatrix} \alpha \\ \beta \end{pmatrix}. \quad (\text{C4})$$

The corresponding Dirac equation reads

$$\begin{pmatrix} \tilde{m}^-(\mathbf{k}) - \mu - \varepsilon & v^+ k_+ e^{-i\theta} \\ v^+ k_- e^{i\theta} & -\tilde{m}^-(\mathbf{k}) - \mu - \varepsilon \end{pmatrix} \psi(\mathbf{r}) = 0. \quad (\text{C5})$$

Notice that the replacement  $k_{\perp} = -i\partial_{x_{\perp}} \rightarrow -i\zeta$  can be made in the equation above. It becomes

$$\begin{pmatrix} m_k - m\zeta^2 - \mu - \varepsilon & i v^+ (k_{\parallel} - \zeta) e^{-i\theta} \\ -i v^+ (k_{\parallel} + \zeta) e^{i\theta} & -(m_k - m\zeta^2) - \mu - \varepsilon \end{pmatrix} \begin{pmatrix} \alpha \\ \beta \end{pmatrix} = 0, \quad (\text{C6})$$

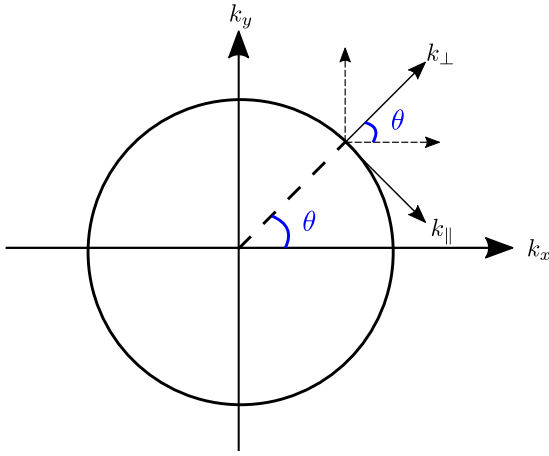


FIG. 5. Relation between  $(k_x, k_y)$  and  $(k_{\parallel}, k_{\perp})$  at a given angle  $\theta$  in the  $k_x k_y$  plane. The coordinate transformation allows us to calculate the boundary states at any  $\theta$  in the  $xy$  plane parametrized by the phase shift  $\phi$  of CPL.

where  $m_k = \tilde{m}_0 + mk_{\parallel}^2$  with  $\tilde{m}_0 = m_0 + m\mathcal{I} - \frac{v^2\mathcal{I}}{\omega} \cos \phi$ . A nontrivial solution of  $(\alpha, \beta)^T$  yields

$$m^2\zeta^4 + (-v^{+2} - 2mm_k)\zeta^2 + v^{+2}k_{\parallel}^2 + m_k^2 - (\varepsilon + \mu)^2 = 0. \quad (\text{C7})$$

The solutions of  $\zeta$  can be found analytically:

$$\zeta_{\pm}^2 = \frac{v^{+2} + 2mm_k}{2m^2} \pm \frac{\sqrt{(v^{+2} + 2mm_k)^2 - 4m^2(v^{+2}k_{\parallel}^2 + m_k^2 - \varepsilon^2)}}{2m^2}. \quad (\text{C8})$$

Note that for the moment we absorb  $\mu$  in  $\varepsilon$  for convenience. The corresponding eigen wave function is

$$\psi_{\zeta}(\mathbf{x}) = e^{ik_{\parallel}x_{\parallel}} e^{\zeta x_{\perp}} \begin{pmatrix} m_k - m\zeta^2 + \varepsilon \\ -iv^{+}(k_{\parallel} + \zeta)e^{i\theta} \end{pmatrix}. \quad (\text{C9})$$

The wave function of boundary states can be written as

$$\Psi(\mathbf{r}) = \sum_{\zeta} C_{\zeta} \psi_{\zeta}(\mathbf{r}). \quad (\text{C10})$$

We impose hard-wall boundary conditions. Thus, the wave function must satisfy

$$\psi(x_{\perp} = 0) = \psi(x_{\perp} \rightarrow \infty) = 0. \quad (\text{C11})$$

Plugging Eq. (C9) into Eq. (C11), this leads to

$$C_{\zeta_1} \begin{pmatrix} m_k - m\zeta_1^2 + \varepsilon \\ -iv^{+}(k_{\parallel} + \zeta_1)e^{i\theta} \end{pmatrix} + C_{\zeta_2} \begin{pmatrix} m_k - m\zeta_2^2 + \varepsilon \\ -iv^{+}(k_{\parallel} + \zeta_2)e^{i\theta} \end{pmatrix} = 0.$$

Solving the boundary equations, we find the energy dispersion of the boundary states as

$$\varepsilon(k_{\parallel}) = \text{sgn}(m)|v^{+}|k_{\parallel}, \quad (\text{C12})$$

and correspondingly, the wave function as

$$\Psi(\mathbf{r}) = \mathcal{N} e^{ik_{\parallel}x_{\parallel}} (e^{\zeta_1 x_{\perp}} - e^{\zeta_2 x_{\perp}}) \begin{pmatrix} \text{sgn}(mv^{+}) \\ -ie^{i\theta} \end{pmatrix}, \quad (\text{C13})$$

where

$$\zeta_{1(2)} = -\frac{|v^{+}|}{2m} \mp \sqrt{\frac{v^{+2}}{4m^2} + \frac{m_k}{m}}. \quad (\text{C14})$$

Similarly, we can find the eigenstates and eigenvectors for the lower block of the Hamiltonian. In summary, the eigenenergies for the two blocks are

$$\begin{aligned} E_{e\uparrow}(k_{\parallel}) &= \text{sgn}(m)|v^{+}|k_{\parallel} - \mu, \\ E_{h\downarrow}(k_{\parallel}) &= -\text{sgn}(m)|v^{-}|k_{\parallel} + \mu, \end{aligned} \quad (\text{C15})$$

respectively, and their eigenvectors in the full basis are

$$\begin{aligned} \Psi_{e\uparrow}(\mathbf{x}) &= F^{+}(\mathbf{x})/\sqrt{2}[\text{sgn}(mv^{+}), -ie^{i\theta}, 0, 0]^T, \\ \Psi_{e\downarrow}(\mathbf{x}) &= F^{-}(\mathbf{x})/\sqrt{2}[0, 0, \text{sgn}(mv^{-}), -ie^{i\theta}]^T, \end{aligned} \quad (\text{C16})$$

where  $F^{\pm}(\mathbf{x}) = \mathcal{N}^{\pm} e^{ik_{\parallel}x_{\parallel}} (e^{\zeta_1^{\pm}x_{\perp}} - e^{\zeta_2^{\pm}x_{\perp}})$  and  $\mathcal{N}^{\pm}$  is the normalization factor, with  $\zeta_{1(2)}^{+/-} = -|(v^{+/-})/2m| \mp \sqrt{(v^{+/-})^2/4m^2 + m_k/m}$ . Without loss of generality, we have taken  $m > 0$  in the following.

After the projection, the effective boundary Hamiltonian can be obtained as

$$h_{\text{eff}}(\theta) = \begin{pmatrix} |v^{+}|k_{\parallel} - \mu & \tilde{\Delta}(\theta) \\ \tilde{\Delta}(\theta)^* & -|v^{-}|k_{\parallel} + \mu \end{pmatrix}. \quad (\text{C17})$$

Here, the basis is  $(\Psi_{e\uparrow}, \Psi_{h\downarrow})$  and the projected pairing potential can be written as

$$\tilde{\Delta}(\theta) = \frac{i}{2} \mathcal{F} \Delta_0 \text{sgn}(v^{-}) [\text{sgn}(v^{+}v^{-})e^{i\theta} - e^{-i\theta}], \quad (\text{C18})$$

where  $\mathcal{F}$  results from the overlap of  $F^{+}(\mathbf{x})$  and  $F^{-}(\mathbf{x})$ .

Inversion symmetry is preserved in the boundary Hamiltonian. After the projection, the symmetry operator becomes

$$\tilde{\mathcal{P}} = \sigma_x. \quad (\text{C19})$$

The boundary Hamiltonian is invariant under inversion,

$$\tilde{\mathcal{P}} h_{\text{eff}}(\theta) \tilde{\mathcal{P}}^{-1} = h_{\text{eff}}(\theta + \pi), \quad (\text{C20})$$

which requires the effective pairing potential to satisfy the following relation:

$$\tilde{\Delta}(\theta + \pi) = -\tilde{\Delta}(\theta). \quad (\text{C21})$$

#### APPENDIX D: MAJORANA ZERO MODES AND THEIR SPIN POLARIZATION

In this section, we derive the wave functions and spin polarizations of Majorana zero modes in the second-order topological phases. We start with the effective boundary Hamiltonian described in Eq. (C17).

The Majorana zero modes are localized exponentially at the positions with vanishing  $\tilde{\Delta}(\theta_0) = 0$  at the boundary. We make the ansatz for the wave function as

$$\Psi = e^{\zeta\iota} \begin{pmatrix} c_1 \\ c_2 \end{pmatrix}, \quad (\text{D1})$$

where  $\iota$  denotes the distance away from one out of these positions. With the replacement  $k_{\parallel} = -i\partial_{\iota} \rightarrow -i\zeta$ , the eigenequation for the zero-energy mode reads

$$\begin{pmatrix} -i|v^{+}|\zeta - \mu & \tilde{\Delta}(\theta) \\ \tilde{\Delta}(\theta)^* & i|v^{-}|\zeta + \mu \end{pmatrix} \begin{pmatrix} c_1 \\ c_2 \end{pmatrix} = 0. \quad (\text{D2})$$



This yields a secular equation

$$|v^+v^-|\zeta^2 - i\mu(|v^+| + |v^-|)\zeta - |\tilde{\Delta}(\theta)|^2 - \mu^2 = 0, \quad (\text{D3})$$

where  $|\tilde{\Delta}(\theta)| = \frac{\sqrt{2}}{2}\mathcal{F}\Delta_0\sqrt{1 - \text{sgn}(v^+v^-)\cos(2\theta)}$ .

Consider  $\mu = 0$ . The two solutions of  $\zeta$  to the above equation are found as

$$\zeta_{\pm} = \pm \frac{|\tilde{\Delta}(\theta)|}{\sqrt{|v^+v^-|}}. \quad (\text{D4})$$

The corresponding eigen wave functions are

$$\begin{pmatrix} c_1 \\ c_2 \end{pmatrix} = \begin{pmatrix} \tilde{\Delta}(\theta)/|\tilde{\Delta}(\theta)| \\ \pm i\sqrt{|v^+/v^-|} \end{pmatrix}. \quad (\text{D5})$$

Near the given position  $\theta_0$  satisfying  $\tilde{\Delta}(\theta_0) = 0$ , we approximate  $\tilde{\Delta}(\theta)/|\tilde{\Delta}(\theta)| = e^{i\theta_0}\text{sgn}(v^+\delta\theta)$ , where  $\delta\theta = \theta - \theta_0$ . Thus, the eigen wave functions become

$$\begin{pmatrix} c_1 \\ c_2 \end{pmatrix} = \begin{pmatrix} e^{i\theta_0}\text{sgn}(v^+\delta\theta) \\ \pm i\sqrt{|v^+/v^-|} \end{pmatrix}. \quad (\text{D6})$$

Notice that  $\zeta_{\pm} = \pm\xi$  with  $\xi > 0$ . Close to the position  $\theta_0$ , the wave function of the zero-energy mode can be written as

$$\begin{aligned} \Psi_{>} &= \alpha e^{-\xi\iota} \begin{pmatrix} e^{i\theta_0}\text{sgn}(v^+) \\ -i\sqrt{|v^+/v^-|} \end{pmatrix}, \quad \theta > \theta_0, \\ \Psi_{<} &= \beta e^{+\xi\iota} \begin{pmatrix} e^{i\theta_0}\text{sgn}(v^+) \\ -i\sqrt{|v^+/v^-|} \end{pmatrix}, \quad \theta < \theta_0. \end{aligned} \quad (\text{D7})$$

Considering the continuity of the wave function at  $\theta = \theta_0$  (i.e.,  $\iota = 0$ ), we obtain  $\alpha = \beta$ . Therefore, the wave function is finally given by

$$\Phi(\theta_0) = \mathcal{K}(\mathbf{r})(e^{i\theta_0}\text{sgn}(v^+)\sqrt{|v^-|}, -i\sqrt{|v^+|})^T, \quad (\text{D8})$$

where  $\mathcal{K}(\theta)$  accounts for both the spatial distribution and the normalization.

To obtain the wave functions for the Majorana zero modes, we need to consider the full Hamiltonian in Eq. (B11). The procedure from Eq. (C2) to Eq. (D8) of finding the zero-energy modes can be similarly performed for the lower block  $h'(\mathbf{k})$  stated in Eq. (B15). For  $h'(\mathbf{k})$ , the eigenenergies, counterparts of Eq. (C15), are found as

$$\begin{aligned} E_{e\downarrow}(k_{\parallel}) &= -|v^-|k_{\parallel} - \mu, \\ E_{h\uparrow}(k_{\parallel}) &= |v^+|k_{\parallel} + \mu, \end{aligned} \quad (\text{D9})$$

and the corresponding eigenvectors, counterparts of Eq. (C16), are

$$\begin{aligned} \Psi_{e\downarrow}(\mathbf{x}) &= F^+(\mathbf{x})/\sqrt{2}[\text{sgn}(v^-), -ie^{-i\theta}, 0, 0]^T, \\ \Psi_{h\uparrow}(\mathbf{x}) &= F^-(\mathbf{x})/\sqrt{2}[0, 0, \text{sgn}(v^+), -ie^{-i\theta}]^T, \end{aligned} \quad (\text{D10})$$

where  $F^{\pm}(\mathbf{x})$  are the normalization factors.

After projecting the pairing interaction onto the boundary states, the effective boundary Hamiltonian for  $h'(\mathbf{k})$  reads

$$h'_{\text{eff}}(\theta) = \begin{pmatrix} |v^-|k_{\parallel} - \mu & \tilde{\Delta}(\theta) \\ \tilde{\Delta}(\theta)^* & -|v^+|k_{\parallel} + \mu \end{pmatrix}, \quad (\text{D11})$$

in the  $(\Psi_{e\downarrow}, \Psi_{h\uparrow})$ , where the projected pairing potential reads  $\tilde{\Delta}(\theta) = i\mathcal{F}\Delta_0\text{sgn}(v^-)[\text{sgn}(v^+v^-)e^{i\theta} - e^{-i\theta}]/2$ . In a similar way as we did for  $h(\mathbf{k})$ , we find a zero-energy mode with the wave function

$$\Phi'(\theta_0) = \mathcal{K}(\mathbf{r})(e^{i\theta_0}\text{sgn}(v^+)\sqrt{|v^+|}, -i\sqrt{|v^-|})^T. \quad (\text{D12})$$

Using the wave functions in Eqs. (D8) and (D12) for the zero-energy modes, the wave functions for two Majorana zero

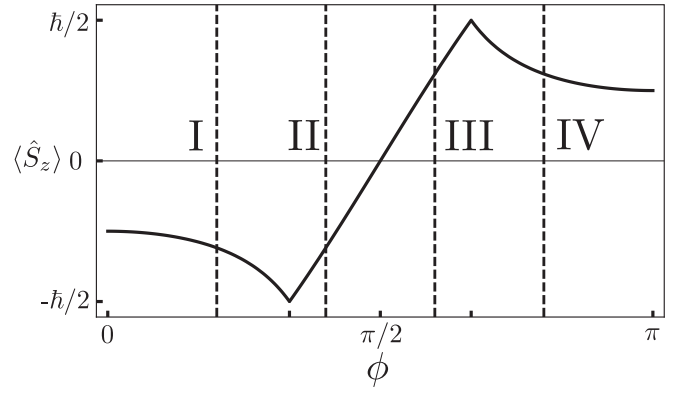


FIG. 6. Spin polarization  $\langle \hat{S}_z \rangle$  against the phase shift  $\phi$  of light for a fixed intensity  $\mathcal{I} = 2(\omega/2m)$ . The four typical examples at I–IV are at  $\phi = 0.2\pi, 0.39\pi, 0.61\pi$ , and  $0.8\pi$ , respectively.

modes at  $\theta = \theta_0$  can be found as

$$\begin{aligned} \Psi_1(\theta_0) &= \mathcal{K}(\mathbf{r}) \begin{pmatrix} e^{i\theta_0}\text{sgn}(v^+)\sqrt{|v^-|} \\ i\sqrt{|v^+|} \\ e^{-i\theta_0}\text{sgn}(v^+)\sqrt{|v^-|} \\ -i\sqrt{|v^+|} \end{pmatrix}, \\ \Psi_2(\theta_0) &= \mathcal{K}(\mathbf{r}) \begin{pmatrix} ie^{i\theta_0}\text{sgn}(v^+)\sqrt{|v^-|} \\ \sqrt{|v^+|} \\ -ie^{-i\theta_0}\text{sgn}(v^+)\sqrt{|v^-|} \\ \sqrt{|v^+|} \end{pmatrix} \end{aligned} \quad (\text{D13})$$

in the full Nambu and spin basis  $(\Psi_{e\uparrow}, \Psi_{e\downarrow}, \Psi_{h\uparrow}, \Psi_{h\downarrow})$ .

With the full wave functions for Majorana zero modes, we next calculate their spin polarization. The  $x$ -component of spin polarization can be calculated by  $\langle \hat{S}_x \rangle_j = \langle \Psi_j | \hat{s}_x | \Psi_j \rangle$ , where  $j \in \{1, 2\}$  and  $\hat{s}_x = \frac{\hbar}{4}(\tau_0 + \tau_z)s_x$ . It is straightforward to find that the two Majorana zero modes have the opposite  $\langle \hat{S}_x \rangle$ ,

$$\langle \hat{S}_x \rangle_j = \frac{\hbar}{2} \frac{(-1)^{j-1} \text{sgn}(v^+)\sqrt{|v^+v^-|} \sin \theta_0}{|v^-| + |v^+|}. \quad (\text{D14})$$

Although the two Majoranas individually may have finite  $\langle \hat{S}_x \rangle$  which depend on the position  $\theta_0$ , they together give vanishing  $\langle \hat{S}_x \rangle$  at the boundary. Similarly, for the  $y$  component of spin polarization given by  $\langle \hat{S}_y \rangle_j = \langle \Psi_j | \hat{s}_y | \Psi_j \rangle$  with  $\hat{s}_y = \frac{\hbar}{4}(\tau_0 + \tau_z)s_y$ , we find opposite values for the two Majoranas,

$$\langle \hat{S}_y \rangle_j = \frac{\hbar}{2} \frac{(-1)^j \text{sgn}(v^+)\sqrt{|v^+v^-|} \cos \theta_0}{|v^-| + |v^+|}. \quad (\text{D15})$$

Thus no net  $\langle \hat{S}_y \rangle$  can be measured at  $\theta = \theta_0$ .

In contrast, for the  $z$  component given by  $\langle \hat{S}_z \rangle_j = \langle \Psi_j | \hat{s}_z | \Psi_j \rangle$  with  $\hat{s}_z = \frac{\hbar}{4}(\tau_0 + \tau_z)s_z$ , the two Majoranas have the same spin polarization,

$$\langle \hat{S}_z \rangle = \frac{\hbar}{2} \frac{|v^-| - |v^+|}{|v^-| + |v^+|}. \quad (\text{D16})$$

Notably, it is independent of the position  $\theta_0$ . Therefore they together allow a finite  $\langle \hat{S}_z \rangle$  which may be probed by magnetic STM. In Fig. 6, we illustrate  $\langle \hat{S}_z \rangle$  for a fixed intensity of light as a function of the phase shift  $\phi$ .

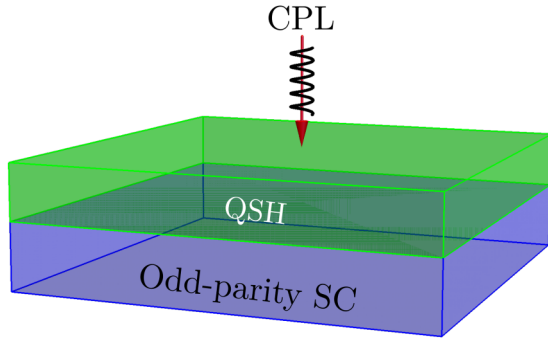


FIG. 7. Sketch of the setup in condensed-matter systems. The circularly polarized light is applied to a quantum spin Hall insulator with proximity-induced odd-parity  $s$ -wave spin-singlet superconductivity.

In the vicinity of  $\phi = \pi/2$ , we denote  $\phi = \pi/2 + \delta\phi$  and perform the series expansion  $\cos(\pi/2 + \delta\phi) \approx -\delta\phi$ . Then we can approximate the corresponding correction as  $v^\pm = v(1 \mp 2m\mathcal{I}\delta\phi/\omega)$ . Hence the spin polarization around  $\pi/2$  can be written as

$$\langle \hat{S}_z \rangle \approx \frac{\hbar}{2} \frac{|1 + \alpha\delta\phi| - |1 - \alpha\delta\phi|}{|1 + \alpha\delta\phi| + |1 - \alpha\delta\phi|} = \frac{2\hbar m\mathcal{I}}{\omega} \delta\phi,$$

where  $\alpha = 2m\mathcal{I}/\omega$ . Clearly, in the vicinity of  $\pi/2$ ,  $\langle \hat{S}_z \rangle$  grows linearly with increasing  $\phi$ .

#### APPENDIX E: CONDENSED-MATTER CANDIDATES

In condensed-matter systems, our proposal can be realized by applying CPL to a QSH insulator with proximity-induced odd-parity  $s$ -wave spin-singlet superconductivity, as shown in Fig. 7. For the material candidates, we note that QSH insulators have been discovered in various materials, for instance, HgTe [81] and monolayer WTe<sub>2</sub> [82]. Odd-parity  $s$ -wave spin-singlet superconductivity has been found, for instance, in iron-based superconductors FeAs/Se [83,84]. Circularly polarized lights have also been applied to manipulate topological superconductors and Majorana zero modes (see, e.g., Ref. [85]).

#### APPENDIX F: COLD-ATOM REALIZATION

The model Hamiltonian in Eq. (1) of the main text can be engineered alternatively using existing technologies in ultracold atoms. Here we take the fermionic <sup>40</sup>K atoms as an example to show its realization. The setup is illustrated in Fig. 8 for the lattice model of Eq. (1) in the main text. We choose the two lowest hyperfine levels,  $|F, m_F\rangle = |9/2, -9/2\rangle$  and  $|9/2, -7/2\rangle$ , as pseudospins, and consider the atomic gases loaded into a bilayer structure. The two layers are stacked along  $z$  direction, and their index mimics the orbital degrees of freedom. In each layer, the atoms are confined in the two-dimensional optical lattice with the trap potential,  $V_L(\mathbf{r}) = V_L[\sin^2(k_L x) + \sin^2(k_L y)]$ . The atoms are prepared to be half filled and thus  $\mu = 0$ .  $V_L$  is the trap strength,  $k_L = \pi/d$ , and  $d$  is optical lattice constant. In order to generate an orbital dependent hopping, we employ the laser-assisted tunneling technique [86,87]. The prepara-

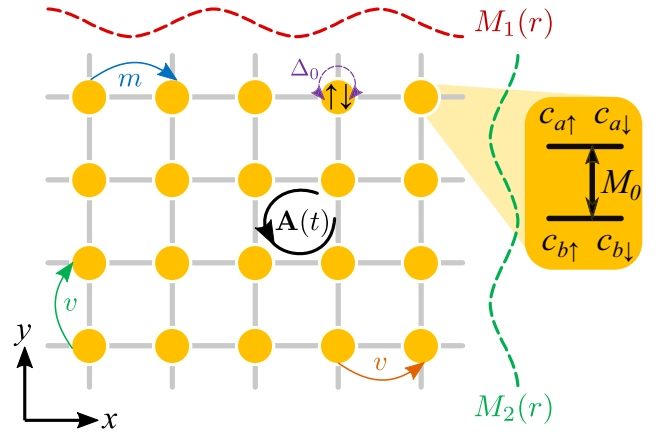


FIG. 8. Model setup projected in the  $x$ - $y$  plane: (i) the nearest-neighbor hopping  $m$  (blue arrow); (ii) orbit coupling  $v$  in  $x$  (red arrow) and  $y$  (green arrow) directions generated by optical fields  $M_1(\mathbf{r})$  and  $M_2(\mathbf{r})$ , respectively; (iii) on-site pairing  $\Delta_0$  (purple arrow); and (iv) effective vector potential  $\mathbf{A}(t)$  (black arrow). As the layer index emulates the orbits, each site is composed of four degrees of freedom in the projection, in which a Zeeman shift  $M_0$  is present.

tion of a spin-dependent magnetic gradient in this technique can simultaneously give rise to an orbital dependent Zeeman shift  $M_0 s_z \sigma_z$  that locally acts on atoms. The original nearest-neighbor hoppings are prominently suppressed due to the magnetic gradient. However, the intralayer one can be restored by using counterpropagating lasers that drive a transition between atoms in adjacent sites via an intermediate excited level, i.e., the laser-assisted tunneling. In the tight-binding model, the above-mentioned terms are expressed as

$$H_0 = \sum_{j,\eta} -m(\Phi_j^\dagger s_z \sigma_0 \Phi_{j+e_\eta} + \text{H.c.}) + M_0 \Phi_j^\dagger s_z \sigma_z \Phi_j, \quad (\text{F1})$$

where  $\Phi_j = (c_{a,j,\uparrow}, c_{b,j,\uparrow}, c_{a,j,\downarrow}, c_{b,j,\downarrow})^T$ ,  $c_{\alpha,j,\beta}$  stands for the annihilation operator for atoms with the orbit  $\alpha \in \{a, b\}$  and spin  $\beta \in \{\uparrow, \downarrow\}$  on the  $j$ th site, and  $\mathbf{e} = (e_x, e_y)$  denotes the unit vector of the lattice. We remark that in Eq. (F1), the hopping is both spin and orbital dependent. In the presence of the spin-dependent magnetic gradient, the relative  $\pi$  phase in the hopping is attainable by initial setups of the counterpropagating lasers.

The orbital coupling in Eq. (1) of the main text can be also synthesized by optical fields. Taking advantage of the selection rules, one can drive a transition between opposite orbits with the same spin via an intermediate level. Such a coupling Hamiltonian is written as

$$H_{\text{oc}} = \int d\mathbf{r} \sum_{\alpha, \alpha' = a, b} \sum_{\beta = \uparrow, \downarrow} i\hat{\Omega}_\beta(\mathbf{r}) \psi_{\alpha, \beta}^\dagger(\mathbf{r}) \psi_{\alpha', \beta}(\mathbf{r}) + \text{H.c.}, \quad (\text{F2})$$

where  $\psi(\mathbf{r})$  denotes the atomic operator in the free space. The effective field mode  $\hat{\Omega}(\mathbf{r})$  can be designed to be spin dependent as [88,89]

$$\hat{\Omega}_\uparrow(\mathbf{r}) = M_1(\mathbf{r}) + iM_2(\mathbf{r}), \quad \hat{\Omega}_\downarrow(\mathbf{r}) = -\hat{\Omega}_\uparrow(\mathbf{r}), \quad (\text{F3})$$

where  $M_1(\mathbf{r}) = \Omega_{\text{eff}} \sin(k_L x) \cos(k_L y) \sin(k_L z)$ ,  $M_2(\mathbf{r}) = \Omega_{\text{eff}} \cos(k_L x) \sin(k_L y) \sin(k_L z)$ , and  $\Omega_{\text{eff}}$  is the effective field strength. Since the Wannier wave function  $W(\mathbf{r})$  is of even parity with respect to each site center, the on-site and intralayer terms in Eq. (F2) vanish. By contrast, the interlayer nearest-neighbor coupling dominates. In the tight-binding model, since the spatial distribution of atoms  $\psi(\mathbf{r})$  is expanded in terms of Wannier wave function  $W(\mathbf{r})$ , Eq. (59) reduces to

$$H_{\text{oc}} = \sum_j i(-1)^{j_x+j_y} \sum_{\beta\beta'} [s_z]_{\beta\beta'} \sum_{\zeta=\pm} \zeta (v_x c_{a,j,\beta}^\dagger c_{b,j+\zeta e_x, \beta'} + i v_y c_{a,j,\beta}^\dagger c_{b,j+\zeta e_y, \beta'}) + \text{H.c.}, \quad (\text{F4})$$

with the effective coupling strength  $v_{x,y}$  determined as  $v_x = \int M_1(\mathbf{r}) W^*(\mathbf{r}) W(\mathbf{r} + d\mathbf{e}_x + d\mathbf{e}_z) d\mathbf{r}$  and  $v_y = \int M_2(\mathbf{r}) W^*(\mathbf{r}) W(\mathbf{r} + d\mathbf{e}_y + d\mathbf{e}_z) d\mathbf{r}$ . Since  $W(\mathbf{r})$  is isotropic in the  $x$ - $y$  plane,  $v_x$  and  $v_y$  are indeed identical. For simplicity, we denote them as  $v_x = v_y \equiv v$ .

In ultracold atoms, the contact interaction is controllable by Feshbach resonances [90]. The interacting Hamiltonian describes a two-body scattering process,

$$H_{\text{int}} = -U \sum_j \sum_\alpha c_{\alpha,j,\uparrow}^\dagger c_{\alpha,j,\downarrow}^\dagger c_{\alpha,j,\downarrow} c_{\alpha,j,\uparrow}, \quad (\text{F5})$$

where  $U = g \int |W(\mathbf{r})|^4 d\mathbf{r}$ , and  $g$  is the bare interaction strength in the spatial space. In the mean-field Bogoliubov–de Gennes (BdG) approach, by assuming the order parameter as  $\Delta_0 = U \langle c_{\alpha,j,\downarrow} c_{\alpha,j,\uparrow} \rangle / 2$ , it gives

$$H_{\text{int}} = -2\Delta_0 \sum_j (c_{a,j,\uparrow}^\dagger c_{a,j,\downarrow}^\dagger + c_{b,j,\uparrow}^\dagger c_{b,j,\downarrow}^\dagger) + \text{H.c.} \quad (\text{F6})$$

We note that a phase of a checkerboard pattern  $(-1)^{j_x+j_y}$  exists in Eq. (F4), which originates from the spatial configuration of the optical field modes (F3). In order to remove it, we make the following operator representation:

$$\begin{aligned} c_{a,j,\downarrow} &\rightarrow c_{b,j,\downarrow}, \\ c_{b,j,\downarrow} &\rightarrow c_{a,j,\downarrow} (-1)^{j_x+j_y}, \\ c_{b,j,\uparrow} &\rightarrow c_{b,j,\uparrow} (-1)^{j_x+j_y}, \end{aligned} \quad (\text{F7})$$

which does not violate the anticommutation relation of operators  $c$ 's. Under the representation in Eq. (F7), Eqs. (F1), (F4), and (F6) are mapped to

$$H_0 = \sum_{j,\eta} [-m(\Phi_j^\dagger s_0 \sigma_z \Phi_{j+e_\eta} + \text{H.c.}) + M_0 \Phi_j^\dagger s_0 \sigma_z \Phi_j], \quad (\text{F8})$$

$$H_{\text{oc}} = \sum_j i v \sum_{\beta\beta'} [s_z]_{\beta\beta'} \sum_{\zeta=\pm} (\zeta c_{a,j,\beta}^\dagger c_{b,j+\zeta e_x, \beta'} + i c_{a,j,\beta}^\dagger c_{b,j+\zeta e_y, \beta'}) + \text{H.c.}, \quad (\text{F9})$$

$$H_{\text{int}} = -2\Delta_0 \sum_j (c_{a,j,\uparrow}^\dagger c_{b,j,\downarrow}^\dagger + c_{b,j,\uparrow}^\dagger c_{a,j,\downarrow}^\dagger) + \text{H.c.} \quad (\text{F10})$$

Combining Eqs. (F1), (F4), and (F6), we obtain the total Hamiltonian as

$$H_{\text{total}} = H_0 + H_{\text{oc}} + H_{\text{int}}. \quad (\text{F11})$$

Performing the Fourier transformation, one can find that the Hamiltonian, Eq. (F11), is identical to the model Hamiltonian, Eq. (1), of the main text.

The vector potential  $\mathbf{A}$  can be introduced via a tilt driving potential in the  $x$ - $y$  plane [91] whose mode is

$$H_{\text{dr}} = \int d\mathbf{r} \sum_{\alpha,\beta} V_{\text{dr}} \psi_{\alpha,\beta}^\dagger(\mathbf{r}) [-x \sin(\omega t) + y \cos(\omega t + \phi)] \psi_{\alpha,\beta}(\mathbf{r}). \quad (\text{F12})$$

In the tight-binding lattice space, it reads

$$H_{\text{dr}} = \sum_{j,\alpha,\beta} V_{\text{dr}} d [-j_x \sin(\omega t) + j_y \cos(\omega t + \phi)] c_{\alpha,j,\beta}^\dagger c_{\alpha,j,\beta}. \quad (\text{F13})$$

By performing the unitary rotation  $\hat{U} = \exp\{i \sum_{j,\alpha,\beta} \frac{V_{\text{dr}} d}{\omega} [j_x \cos(\omega t) + j_y \sin(\omega t + \phi)] c_{\alpha,j,\beta}^\dagger c_{\alpha,j,\beta}\}$ , the effective Hamiltonian in the rotated frame is obtained as  $H_{\text{eff}} = \hat{U} H_{\text{total}} \hat{U}^\dagger - i \hat{U} \partial_t \hat{U}^\dagger$ . This will leave a global phase  $V_{\text{dr}} d \cos(\omega t) / \omega$  in  $x$  direction, while  $V_{\text{dr}} d \sin(\omega t + \phi) / \omega$  in  $y$  direction, to the hopping and orbit-coupling terms, which emulates the Peierls phase. According to the vector potential defined in the main text, in this simulation scheme,  $\mathbf{A}$  is approximated as

$$\mathbf{A} = A_0 [\cos(\omega t), \sin(\omega t + \phi), 0], \quad A_0 = V_{\text{dr}} / \omega. \quad (\text{F14})$$

## APPENDIX G: EXPERIMENTAL SUGGESTIONS

In this section we give experimental suggestions and realistic parameters for the cold-atom experiment. In the model Hamiltonian, Eq. (1), of the main text, the normal part described by  $\mathcal{H}_0 = [M_0 - 2m(\cos k_x + \cos k_y)] \tau_z \sigma_z + v \sin k_x s_z \sigma_x + v \sin k_y \tau_z \sigma_y$  is essentially a QSH insulator model. For simplicity, we focus on the phase transition induced by the gap closing around the  $\Gamma$  point [i.e.,  $(k_x, k_y) = (0, 0)$ ]. The model is nontrivial in the region of  $M_0 - 4m < 0$ , with the energy gap  $E_{\text{gap}} = 2|M_0 - 4m|$ . Thus  $M_0$  shall be in the range of  $M_0 < 4m$ . The pairing interaction  $h_\Delta$  is responsible for generating the higher-order topological phase, which shall not break the original QSH phase by closing the bulk gap. Thus it is required that  $\Delta_0 < E_{\text{gap}} = 2|M_0 - 4m|$ .

For the periodic vector potential  $\mathbf{A}(t)$ , its frequency shall be greater than the width of the static energy band. For typical Floquet experiments, the frequency is taken approximately in the same order as the nearest-neighbor hopping magnitude  $m$  [92,93]. According to the phase diagram in Fig. 4(a) in the main text, to induce Weyl points, the intensity  $\mathcal{I} = e^2 A_0^2$  shall be larger than  $\omega / (2m)$ .

Next we proceed to give a set of parameters fulfilling these requirements, which are accessible in cold-atom experiments. In practice, the optical lattice is created by counterpropagating  $\lambda_L = 1064$ -nm lasers, with the lattice constant  $d = \lambda_L / 2$  and the recoil energy  $E_R = \hbar^2 / (2m_{\text{atom}} \lambda_L^2) \approx 212$  nK. We set the trap depth of the optical lattice as  $V_L = 5E_R$ , and the corresponding nearest-neighbor hopping magnitude is  $m = 0.093E_R$ . By preparing the effective field strength as  $\Omega_{\text{eff}} = 40E_R$ , we can obtain the generated orbit coupling  $v \approx 0.74m$ . The onsite potential can be tuned as  $M_0 = 2.20m$ . By setting the bare interaction strength  $g = 0.016E_R$ , we acquire the order parameter  $\Delta_0 \approx 0.35m$ , fulfilling the requirements. For engineering the vector potential  $\mathbf{A}(t)$ , we set the

TABLE I. Realistic parameters to be explored experimentally. Here  $m = 0.093E_R = 19.716$  nK is taken as the unit.

Unit	$m$	$M_0$	$v$	$\Delta_0$	$\hbar\omega$	$A_0$
$\times 19.716$ nK	1.00	2.20	0.74	0.35	1.10	$1.80 \mu\text{m}^{-1}$

- [1] C.-K. Chiu, J. C. Y. Teo, A. P. Schnyder, and S. Ryu, Classification of topological quantum matter with symmetries, *Rev. Mod. Phys.* **88**, 035005 (2016).
- [2] G. E. Volovik, *Universe in a Helium Droplet* (Oxford University Press, Oxford, England, 2003).
- [3] Y. X. Zhao and Z. D. Wang, Topological Classification and Stability of Fermi Surfaces, *Phys. Rev. Lett.* **110**, 240404 (2013).
- [4] M. Sato and S. Fujimoto, Majorana fermions and topology in superconductors, *J. Phys. Soc. Jpn.* **85**, 072001 (2016).
- [5] M. Sato and Y. Ando, Topological superconductors: A review, *Rep. Prog. Phys.* **80**, 076501 (2017).
- [6] N. P. Armitage, E. J. Mele, and A. Vishwanath, Weyl and Dirac semimetals in three-dimensional solids, *Rev. Mod. Phys.* **90**, 015001 (2018).
- [7] Y. Tanaka, M. Sato, and N. Nagaosa, Symmetry and topology in superconductors odd-frequency pairing and edge states, *J. Phys. Soc. Jpn.* **81**, 011013 (2012).
- [8] X. Wan, A. M. Turner, A. Vishwanath, and S. Y. Savrasov, Topological semimetal and Fermi-arc surface states in the electronic structure of pyrochlore iridates, *Phys. Rev. B* **83**, 205101 (2011).
- [9] S.-Y. Xu, I. Belopolski, N. Alidoust, M. Neupane, G. Bian, C. Zhang, R. Sankar, G. Chang, Z. Yuan, C.-C. Lee, S.-M. Huang, H. Zheng, J. Ma, D. S. Sanchez, B. Wang, A. Bansil, F. Chou, P. P. Shibayev, H. Lin, S. Jia, and M. Z. Hasan, Discovery of a Weyl fermion semimetal and topological Fermi arcs, *Science* **349**, 613 (2015).
- [10] Z. K. Liu, J. Jiang, B. Zhou, Z. J. Wang, Y. Zhang, H. M. Weng, D. Prabhakaran, S.-K. Mo, H. Peng, P. Dudin, T. Kim, M. Hoesch, Z. Fang, X. Dai, Z. X. Shen, D. L. Feng, Z. Hussain, and Y. L. Chen, A stable three-dimensional topological Dirac semimetal  $\text{Cd}_3\text{As}_2$ , *Nat. Mater.* **13**, 677 (2014).
- [11] T. Meng and L. Balents, Weyl superconductors, *Phys. Rev. B* **86**, 054504 (2012).
- [12] S. A. Yang, H. Pan, and F. Zhang, Dirac and Weyl Superconductors in Three Dimensions, *Phys. Rev. Lett.* **113**, 046401 (2014).
- [13] W. B. Rui, M. M. Hirschmann, and A. P. Schnyder,  $\mathcal{PT}$ -symmetric non-Hermitian Dirac semimetals, *Phys. Rev. B* **100**, 245116 (2019).
- [14] N. Morali, R. Batabyal, P. K. Nag, E. Liu, Q. Xu, Y. Sun, B. Yan, C. Felser, N. Avraham, and H. Beidenkopf, Fermi-arc diversity on surface terminations of the magnetic Weyl semimetal  $\text{Co}_3\text{Sn}_2\text{S}_2$ , *Science* **365**, 1286 (2019).
- [15] D. F. Liu, A. J. Liang, E. K. Liu, Q. N. Xu, Y. W. Li, C. Chen, D. Pei, W. J. Shi, S. K. Mo, P. Dudin, T. Kim, C. Cacho, G. Li, Y. Sun, L. X. Yang, Z. K. Liu, S. S. P. Parkin, C. Felser, and Y. L. Chen, Magnetic Weyl semimetal phase in a kagomé crystal, *Science* **365**, 1282 (2019).
- [16] W. A. Benalcazar, B. A. Bernevig, and T. L. Hughes, Quantized electric multipole insulators, *Science* **357**, 61 (2017).
- [17] Z. Song, Z. Fang, and C. Fang,  $(d-2)$ -Dimensional Edge States of Rotation Symmetry Protected Topological States, *Phys. Rev. Lett.* **119**, 246402 (2017).
- [18] J. Langbehn, Y. Peng, L. Trifunovic, F. von Oppen, and P. W. Brouwer, Reflection-Symmetric Second-Order Topological Insulators and Superconductors, *Phys. Rev. Lett.* **119**, 246401 (2017).
- [19] C. W. Peterson, T. Li, W. A. Benalcazar, T. L. Hughes, and G. Bahl, A fractional corner anomaly reveals higher-order topology, *Science* **368**, 1114 (2020).
- [20] F. Schindler, A. M. Cook, M. G. Vergniory, Z. Wang, S. S. P. Parkin, B. A. Bernevig, and T. Neupert, Higher-order topological insulators, *Sci. Adv.* **4**, eaat0346 (2018).
- [21] F. Schindler, Z. Wang, M. G. Vergniory, A. M. Cook, A. Murani, S. Sengupta, A. Yu. Kasumov, R. Deblock, S. Jeon, I. Drozdov, H. Bouchiat, S. Gurun, A. Yazdani, B. A. Bernevig, and T. Neupert, Higher-order topology in bismuth, *Nat. Phys.* **14**, 918 (2018).
- [22] M. Serra-Garcia, V. Peri, R. Süsstrunk, O. R. Bilal, T. Larsen, L. G. Villanueva, and S. D. Huber, Observation of a phononic quadrupole topological insulator, *Nature (London)* **555**, 342 (2018).
- [23] M. Ezawa, Higher-Order Topological Insulators and Semimetals on the Breathing Kagome and Pyrochlore Lattices, *Phys. Rev. Lett.* **120**, 026801 (2018).
- [24] L. Trifunovic and P. W. Brouwer, Higher-Order Bulk-Boundary Correspondence for Topological Crystalline Phases, *Phys. Rev. X* **9**, 011012 (2019).
- [25] R. Chen, C.-Z. Chen, J.-H. Gao, B. Zhou, and D.-H. Xu, Higher-Order Topological Insulators in Quasicrystals, *Phys. Rev. Lett.* **124**, 036803 (2020).
- [26] E. Khalaf, Higher-order topological insulators and superconductors protected by inversion symmetry, *Phys. Rev. B* **97**, 205136 (2018).
- [27] R.-J. Slager, L. Rademaker, J. Zaanen, and L. Balents, Impurity-bound states and Green's function zeros as local signatures of topology, *Phys. Rev. B* **92**, 085126 (2015).
- [28] D. Călugăru, V. Juričić, and B. Roy, Higher-order topological phases: A general principle of construction, *Phys. Rev. B* **99**, 041301(R) (2019).
- [29] M. Lin and T. L. Hughes, Topological quadrupolar semimetals, *Phys. Rev. B* **98**, 241103(R) (2018).
- [30] R.-X. Zhang, Y.-T. Hsu, and S. Das Sarma, Higher-order topological Dirac superconductors, *Phys. Rev. B* **102**, 094503 (2020).
- [31] H.-X. Wang, Z.-K. Lin, B. Jiang, G.-Y. Guo, and J.-H. Jiang, Higher-Order Weyl Semimetals, *Phys. Rev. Lett.* **125**, 146401 (2020).
- [32] S. A. A. Ghorashi, X. Hu, T. L. Hughes, and E. Rossi, Second-order Dirac superconductors and magnetic field



- induced Majorana hinge modes, *Phys. Rev. B* **100**, 020509(R) (2019).
- [33] S. A. A. Ghorashi, T. Li, and T. L. Hughes, Higher-Order Weyl Semimetals, *Phys. Rev. Lett.* **125**, 266804 (2020).
- [34] K. Wang, J.-X. Dai, L. B. Shao, S. A. Yang, and Y. X. Zhao, Boundary Criticality of  $\mathcal{PT}$ -Invariant Topology and Second-Order Nodal-Line Semimetals, *Phys. Rev. Lett.* **125**, 126403 (2020).
- [35] A. Tiwari, A. Jahin, and Y. Wang, Chiral Dirac superconductors: Second-order and boundary-obstructed topology, *Phys. Rev. Research* **2**, 043300 (2020).
- [36] B. Roy, Antiunitary symmetry protected higher-order topological phases, *Phys. Rev. Research* **1**, 032048(R) (2019).
- [37] G. Y. Cho, J. H. Bardarson, Y.-M. Lu, and J. E. Moore, Superconductivity of doped Weyl semimetals: Finite-momentum pairing and electronic analog of the  $^3\text{He-}a$  phase, *Phys. Rev. B* **86**, 214514 (2012).
- [38] G. Bednik, A. A. Zyuzin, and A. A. Burkov, Superconductivity in Weyl metals, *Phys. Rev. B* **92**, 035153 (2015).
- [39] P. K. Biswas, H. Luetkens, T. Neupert, T. Stürzer, C. Baines, G. Pascua, A. P. Schnyder, M. H. Fischer, J. Goryo, M. R. Lees, H. Maeter, F. Brückner, H.-H. Klauss, M. Nicklas, P. J. Baker, A. D. Hillier, M. Sigrist, A. Amato, and D. Johrendt, Evidence for superconductivity with broken time-reversal symmetry in locally noncentrosymmetric SrPtAs, *Phys. Rev. B* **87**, 180503(R) (2013).
- [40] M. H. Fischer, T. Neupert, C. Platt, A. P. Schnyder, W. Hanke, J. Goryo, R. Thomale, and M. Sigrist, Chiral  $d$ -wave superconductivity in SrPtAs, *Phys. Rev. B* **89**, 020509(R) (2014).
- [41] P. Goswami and L. Balicas, Topological properties of possible Weyl superconducting states of  $\text{UrU}_2\text{Si}_2$ , [arXiv:1312.3632](https://arxiv.org/abs/1312.3632).
- [42] I. M. Hayes, D. S. Wei, T. Metz, J. Zhang, Y. S. Eo, S. Ran, S. R. Saha, J. Collini, N. P. Butch, D. F. Agterberg, A. Kapitulnik, and J. Paglionee, Weyl superconductivity in  $\text{UTe}_2$ , [arXiv:2002.02539](https://arxiv.org/abs/2002.02539).
- [43] W. Wang, S. Kim, M. Liu, F. A. Cevallos, R. J. Cava, and N. P. Ong, Evidence for an edge supercurrent in the Weyl superconductor  $\text{MoTe}_2$ , *Science* **368**, 534 (2020).
- [44] T. Yamashita, Y. Shimoyama, Y. Haga, T. D. Matsuda, E. Yamamoto, Y. Onuki, H. Sumiyoshi, S. Fujimoto, A. Levchenko, T. Shibauchi, and Y. Matsuda, Colossal thermomagnetic response in the exotic superconductor  $\text{URu}_2\text{Si}_2$ , *Nat. Phys.* **11**, 17 (2015).
- [45] Y. Yanase and K. Shiozaki, Möbius topological superconductivity in  $\text{UPt}_3$ , *Phys. Rev. B* **95**, 224514 (2017).
- [46] Y. Yanase, Nonsymmorphic Weyl superconductivity in  $\text{UPt}_3$  based on  $E_{2u}$  representation, *Phys. Rev. B* **94**, 174502 (2016).
- [47] N. F. Q. Yuan, W.-Y. He, and K. T. Law, Superconductivity-induced ferromagnetism and Weyl superconductivity in Nb-doped  $\text{Bi}_2\text{Se}_3$ , *Phys. Rev. B* **95**, 201109(R) (2017).
- [48] C.-H. Hsu, P. Stano, J. Klinovaja, and D. Loss, Majorana Kramers Pairs in Higher-Order Topological Insulators, *Phys. Rev. Lett.* **121**, 196801 (2018).
- [49] T. Liu, J. J. He, and F. Nori, Majorana corner states in a two-dimensional magnetic topological insulator on a high-temperature superconductor, *Phys. Rev. B* **98**, 245413 (2018).
- [50] Z. Yan, F. Song, and Z. Wang, Majorana Corner Modes in a High-Temperature Platform, *Phys. Rev. Lett.* **121**, 096803 (2018).
- [51] Q. Wang, C.-C. Liu, Y.-M. Lu, and F. Zhang, High-Temperature Majorana Corner States, *Phys. Rev. Lett.* **121**, 186801 (2018).
- [52] X. Zhu, Tunable Majorana corner states in a two-dimensional second-order topological superconductor induced by magnetic fields, *Phys. Rev. B* **97**, 205134 (2018).
- [53] X. Zhu, Second-Order Topological Superconductors with Mixed Pairing, *Phys. Rev. Lett.* **122**, 236401 (2019).
- [54] M. Geier, L. Trifunovic, M. Hoskam, and P. W. Brouwer, Second-order topological insulators and superconductors with an order-two crystalline symmetry, *Phys. Rev. B* **97**, 205135 (2018).
- [55] Z. Yan, Higher-Order Topological Odd-Parity Superconductors, *Phys. Rev. Lett.* **123**, 177001 (2019).
- [56] Y. Volpez, D. Loss, and J. Klinovaja, Second-Order Topological Superconductivity in  $\pi$ -Junction Rashba Layers, *Phys. Rev. Lett.* **122**, 126402 (2019).
- [57] R.-X. Zhang, W. S. Cole, and S. Das Sarma, Helical Hinge Majorana Modes in Iron-Based Superconductors, *Phys. Rev. Lett.* **122**, 187001 (2019).
- [58] S.-B. Zhang and B. Trauzettel, Detection of second-order topological superconductors by Josephson junctions, *Phys. Rev. Research* **2**, 012018(R) (2020).
- [59] K. Plekhanov, M. Thakurathi, D. Loss, and J. Klinovaja, Floquet second-order topological superconductor driven via ferromagnetic resonance, *Phys. Rev. Research* **1**, 032013(R) (2019).
- [60] Y.-J. Wu, J. Hou, Y.-M. Li, X.-W. Luo, X. Shi, and C. Zhang, In-Plane Zeeman-Field-Induced Majorana Corner and Hinge Modes in an  $s$ -Wave Superconductor Heterostructure, *Phys. Rev. Lett.* **124**, 227001 (2020).
- [61] X.-H. Pan, K.-J. Yang, L. Chen, G. Xu, C.-X. Liu, and X. Liu, Lattice-Symmetry-Assisted Second-Order Topological Superconductors and Majorana Patterns, *Phys. Rev. Lett.* **123**, 156801 (2019).
- [62] J. Ahn and B.-J. Yang, Higher-order topological superconductivity of spin-polarized fermions, *Phys. Rev. Research* **2**, 012060(R) (2020).
- [63] S.-B. Zhang, A. Calzona, and B. Trauzettel, All-electrically tunable networks of Majorana bound states, *Phys. Rev. B* **102**, 100503(R) (2020).
- [64] S.-B. Zhang, W. B. Rui, A. Calzona, S.-J. Choi, A. P. Schnyder, and B. Trauzettel, Topological and holonomic quantum computation based on second-order topological superconductors, *Phys. Rev. Research* **2**, 043025 (2020).
- [65] A. Tiwari, M.-H. Li, B. A. Bernevig, T. Neupert, and S. A. Parameswaran, Unhinging the Surfaces of Higher-Order Topological Insulators and Superconductors, *Phys. Rev. Lett.* **124**, 046801 (2020).
- [66] K. Laubscher, D. Loss, and J. Klinovaja, Majorana and parafermion corner states from two coupled sheets of bilayer graphene, *Phys. Rev. Research* **2**, 013330 (2020).
- [67] Y.-T. Hsu, W. S. Cole, R.-X. Zhang, and J. D. Sau, Inversion-Protected Higher-Order Topological Superconductivity in Monolayer  $\text{WTe}_2$ , *Phys. Rev. Lett.* **125**, 097001 (2020).
- [68] X. Wu, X. Liu, R. Thomale, and C.-X. Liu, High- $T_c$  superconductor  $\text{Fe}(\text{Se},\text{Te})$  monolayer: An intrinsic, scalable and electrically-tunable majorana platform, [arXiv:1905.10648](https://arxiv.org/abs/1905.10648).
- [69] Y. Peng, Floquet higher-order topological insulators and superconductors with space-time symmetries, *Phys. Rev. Research* **2**, 013124 (2020).

- [70] R. W. Bomantara and J. Gong, Measurement-only quantum computation with Floquet Majorana corner modes, *Phys. Rev. B* **101**, 085401 (2020).
- [71] R.-X. Zhang, W. S. Cole, X. Wu, and S. Das Sarma, Higher-Order Topology and Nodal Topological Superconductivity in Fe(Se,Te) Heterostructures, *Phys. Rev. Lett.* **123**, 167001 (2019).
- [72] A. P. Schnyder, S. Ryu, A. Furusaki, and A. W. W. Ludwig, Classification of topological insulators and superconductors in three spatial dimensions, *Phys. Rev. B* **78**, 195125 (2008).
- [73] The nonzero Chern number can be understood from the fact that there is an equal number of Weyl points of opposite chirality in each Weyl-point set, rendering the Chern number nonzero only inside each set. Here we refer to the boundary states that have the same origin, like the hinge boundary states, as “hinge Majorana arcs” on a 2D surface.
- [74] Note that the position switching cannot be directly adopted for braiding operations.
- [75] H.-H. Sun, K.-W. Zhang, L.-H. Hu, C. Li, G.-Y. Wang, H.-Y. Ma, Z.-A. Xu, C.-L. Gao, D.-D. Guan, Y.-Y. Li, C. Liu, D. Qian, Y. Zhou, L. Fu, S.-C. Li, F.-C. Zhang, and J.-F. Jia, Majorana Zero Mode Detected with Spin Selective Andreev Reflection in the Vortex of a Topological Superconductor, *Phys. Rev. Lett.* **116**, 257003 (2016).
- [76] S. Jeon, Y. Xie, J. Li, Z. Wang, B. A. Bernevig, and A. Yazdani, Distinguishing a Majorana zero mode using spin-resolved measurements, *Science* **358**, 772 (2017).
- [77] L. Fu and E. Berg, Odd-Parity Topological Superconductors: Theory and Application to  $\text{Cu}_x\text{Bi}_2\text{Se}_3$ , *Phys. Rev. Lett.* **105**, 097001 (2010).
- [78] T. Kitagawa, T. Oka, A. Brataas, L. Fu, and E. Demler, Transport properties of nonequilibrium systems under the application of light: Photoinduced quantum Hall insulators without Landau levels, *Phys. Rev. B* **84**, 235108 (2011).
- [79] N. Goldman and J. Dalibard, Periodically Driven Quantum Systems: Effective Hamiltonians and Engineered Gauge Fields, *Phys. Rev. X* **4**, 031027 (2014).
- [80] C.-T. Hsieh, T. Morimoto, and S. Ryu, CPT theorem and classification of topological insulators and superconductors, *Phys. Rev. B* **90**, 245111 (2014).
- [81] M. König, S. Wiedmann, C. Brüne, A. Roth, H. Buhmann, L. W. Molenkamp, X.-L. Qi, and S.-C. Zhang, Quantum spin Hall insulator state in HgTe quantum wells, *Science* **318**, 766 (2007).
- [82] S. Wu, V. Fatemi, Q. D. Gibson, K. Watanabe, T. Taniguchi, R. J. Cava, and P. Jarillo-Herrero, Observation of the quantum spin Hall effect up to 100 Kelvin in a monolayer crystal, *Science* **359**, 76 (2018).
- [83] J. Hu, Iron-Based Superconductors as Odd-Parity Superconductors, *Phys. Rev. X* **3**, 031004 (2013).
- [84] N. Hao and J. Hu, Topological Phases in the Single-Layer Fese, *Phys. Rev. X* **4**, 031053 (2014).
- [85] M. Claassen, D. M. Kennes, M. Zingl, M. A. Sentef, and A. Rubio, Universal optical control of chiral superconductors and Majorana modes, *Nat. Phys.* **15**, 766 (2019).
- [86] M. Aidelsburger, M. Atala, M. Lohse, J. T. Barreiro, B. Paredes, and I. Bloch, Realization of the Hofstadter Hamiltonian with Ultracold Atoms in Optical Lattices, *Phys. Rev. Lett.* **111**, 185301 (2013).
- [87] H. Miyake, G. A. Siviloglou, C. J. Kennedy, W. C. Burton, and W. Ketterle, Realizing the Harper Hamiltonian with Laser-Assisted Tunneling in Optical Lattices, *Phys. Rev. Lett.* **111**, 185302 (2013).
- [88] X.-J. Liu, K. T. Law, and T. K. Ng, Realization of 2D Spin-Orbit Interaction and Exotic Topological Orders in Cold Atoms, *Phys. Rev. Lett.* **112**, 086401 (2014).
- [89] Z. Wu, L. Zhang, W. Sun, X.-T. Xu, B.-Z. Wang, S.-C. Ji, Y. Deng, S. Chen, X.-J. Liu, and J.-W. Pan, Realization of two-dimensional spin-orbit coupling for Bose-Einstein condensates, *Science* **354**, 83 (2016).
- [90] C. Chin, R. Grimm, P. Julienne, and E. Tiesinga, Feshbach resonances in ultracold gases, *Rev. Mod. Phys.* **82**, 1225 (2010).
- [91] J. Struck, C. Ölschläger, M. Weinberg, P. Hauke, J. Simonet, A. Eckardt, M. Lewenstein, K. Sengstock, and P. Windpassinger, Tunable Gauge Potential for Neutral and Spinless Particles in Driven Optical Lattices, *Phys. Rev. Lett.* **108**, 225304 (2012).
- [92] M. Sentef, M. Claassen, A. Kemper, B. Moritz, T. Oka, J. Freericks, and T. Devereaux, Theory of Floquet band formation and local pseudospin textures in pump-probe photoemission of graphene, *Nat. Commun.* **6**, 7047 (2015).
- [93] X.-S. Li, C. Wang, M.-X. Deng, H.-J. Duan, P.-H. Fu, R.-Q. Wang, L. Sheng, and D. Y. Xing, Photon-Induced Weyl Half-Metal Phase and Spin Filter Effect from Topological Dirac Semimetals, *Phys. Rev. Lett.* **123**, 206601 (2019).